Tectonic and eustatic controls on sequence stratigraphy of the Pliocene Loreto basin, Baja California Sur, Mexico

Rebecca J. Dorsey* *Department of Geological Sciences, 1272 University of Oregon, Eugene, Oregon 97403-1272*
Paul J. Umhoefer† *Department of Geology, Northern Arizona University, Flagstaff, Arizona 86011*

ABSTRACT

The Loreto basin formed by rapid westward tilting and asymmetric subsidence within a broad releasing bend of the Loreto fault during transtensional deformation along the western margin of the active Gulf of California plate boundary. Sedimentary rocks range in age from ~5(?) to 2.0 Ma and consist of siliciclastic and carbonate deposits that accumulated in nonmarine, deltaic, and marine settings. The basin is divided into the central and southeast subbasins, which have distinctly different subsidence histories and stratigraphic evolution. Sedimentary rocks of the Loreto basin are divided into four stratigraphic sequences that record discrete phases of fault-controlled subsidence and basin filling. Sequence boundaries record major changes in tilting geometries and sediment dispersal that were caused by reorganization of basin-bounding faults. Sequence 1 consists of nonmarine conglomerate and sandstone that accumulated in alluvial fans and braided streams. The sequence 1–2 boundary is a marine flooding surface in both subbasins, and parasequences within sequence 2 consist of progradational Gilbert deltas that are capped by transgressive marine shell concentrations and flooding surfaces. The sequence 2–3 boundary is a low-angle erosional unconformity in the southeast subbasin and a thin interval of downlap in the central subbasin. Sequence 3 is characterized by bioclastic limestones that were derived from the uplifted portion of the hanging-wall tilt block. The sequence 3–4 boundary is an angular unconformity in the southeast subbasin and an abrupt marine flooding surface in the central subbasin. Sequence 4 consists dominantly of in situ shallow-marine carbonate deposits.

By comparing parasequences of sequence 2 with marine oxygen-isotope curves, we can discriminate between eustatic and tectonic controls on stratigraphic evolution. In the central subbasin, sequence 2 accumulated during a short phase of extremely rapid subsidence (8 mm/yr); it contains 14 paracycles that do not match the O-isotope curve, and there are no unconformities. In the southeast subbasin, sequence 2 accumulated at a rate of ~1.5 mm/yr; it contains 4 paracycles that appear to match the O-isotope curve, and sequence boundaries are unconformities. Thus, we conclude that during sequence 2 deposition: (1) extremely rapid subsidence in the central subbasin outpaced eustatic sea-level changes, and Gilbert delta paracycles were produced by episodic fault-controlled subsidence; and (2) subsidence in the southeast subbasin was slower than the rate of eustatic sea-level changes, and the internal stratigraphic cyclicity preserves a record of eustatic rather than tectonic events.

*E-mail: rdorsey@darkwing.uoregon.edu.
†E-mail: paul.umhoefer@nau.edu

INTRODUCTION

The stratigraphy of sedimentary basins can be used to reconstruct subsidence histories, evolution of depositional systems, and adjustments to changing parameters of sediment input and accommodation space through time. In tectonically active settings, sediment input and accommodation space are controlled by slip on basin-bounding faults and variations in the rates and geometries of crustal tilting produced by fault slip and/or folding. Active basins undergo complex spatial and temporal variations in subsidence, uplift, sediment dispersal, and source-area erosion, and these variations can produce strikingly different stratigraphic signatures over short distances (e.g., Christie-Blick and Biddle, 1985; Leeder and Gawthorpe, 1987; Gawthorpe and Colella, 1990). The rate of sediment input may vary as a function of changing uplift and erosion patterns in source areas, stream-capture events related to faulting, and/or climatically controlled variations in rainfall and sediment yield (e.g., Heller and Paola, 1992; Koltermann and Gorelick, 1992). In tectonically active marine basins, accommodation space is controlled by the interplay between rate of subsidence (or uplift) and fluctuations in eustatic sea level. In deep half-graben depocenters, for example, rapid steady subsidence may exceed rates of sea-level rise and fall, and preserved stratigraphic cyclicity may record continuous creation of accommodation space modulated by the effects of high-frequency eustatic fluctuations (Gawthorpe et al., 1994, 1997; Dart et al., 1994; Hardy and Gawthorpe, 1998). Although the range of processes that can influence stratigraphy in tectonically active basins is generally well known, identification of those processes based on interpretation of the stratigraphic record is difficult and commonly is hindered by lack of adequate age controls on syntectonic strata.

The Pliocene Loreto basin (Fig. 1) is an excellent setting within which to evaluate controls on stratigraphic evolution of a tectonically active oblique-rift marine basin. The basin fill is well exposed and laterally mappable due to young uplift and exhumation. The age of stratigraphic units is well constrained by high-resolution dating of interbedded tuffs, and the history of faulting within and around the margins of the basin is well known from detailed mapping and fault-kinematic analysis. This paper presents the results of a multiyear study of the Loreto basin that has focused on unraveling complex stratigraphic and structural evolution during a period of rapid slip and subsidence on the basin-bounding Loreto fault. Detailed study of map-scale stratal geometries, lithofacies assemblages, stratigraphic bounding surfaces, and parasequence stacking patterns has enabled us to develop a sequence-stratigraphic framework for interpreting the basin history.

Because of the unique factors that control tectonically active basins, application of sequence stratigraphy in active settings tends to depart from the usage of traditional models, which were developed in passive-margin settings (Vail et al.,

GSA Bulletin; February 2000; v. 112; no. 2; p. 177–199; 16 figures; 3 tables.

1977; Van Wagoner et al., 1988; Jervey, 1988). In areas where rapid tectonic subsidence produces a continual rise in relative sea level, erosional unconformities may be absent and sequence boundaries may be defined by marine flooding surfaces and thin zones of downlap (Gawthorpe et al., 1994; Dart et al., 1994; Burns et al., 1997). Using a modified sequence-stratigraphic framework in the Loreto basin, we are able to determine variations in relative sea level, sediment-dispersal patterns, and the ratio of accommodation production versus sediment input through time. The results of this analysis are useful for comparison with other studies in similar, tectonically active basins where high-resolution age dating may not be possible.

TECTONIC SETTING

The Loreto basin is located on the southwestern margin of the Gulf of California, which has opened during the past 4 to 6 m.y. by transform-rifting along the Pacific–North American plate boundary (Fig. 1; Curray and Moore, 1984; Stock and Hodges, 1989; Lonsdale, 1989). The axial portion of the Gulf of California is dominated by large transform faults connected by short spreading-ridge segments that produce deep nascent oceanic basins; these transform faults connect northward with the San Andreas fault system in southern California (Fig. 1A). Thus, the Gulf of California is an obliquely rifted, proto-oceanic plate boundary along which transform motion is greater than rifting. The Main Gulf Escarpment is a large topographic escarpment, about 0.5–2 km high, that follows the eastern margin of the Baja California peninsula (Fig. 1). Areas west of the Main Gulf Escarpment are underlain by a thick, gently west-dipping and westward-fining assemblage of lower to middle Miocene volcaniclastic sedimentary rocks that were shed from high-standing, subduction-related stratovolcanoes (Hausback, 1984; Stock and Hodges, 1989; Dorsey and Burns, 1994). Areas east of the Main Gulf Escarpment make up the western part of the Gulf extensional province, which is a broad region dominated by structures related to the development of the Gulf of California (Gastil et al., 1975; Stock and Hodges, 1989). The Gulf extensional province in eastern Baja California is a ~0–30-km-wide zone of hills and plains underlain by faulted and tilted Miocene volcanic rocks, local Miocene and Pliocene basinal strata (including the Loreto basin), and local volcanic centers of late Miocene to Quaternary age (Fig. 1). Geologically, the 5–30-km-wide offshore marine shelf and scattered islands in the Gulf of California are the offshore continuation of the Gulf extensional province. Miocene stratigraphy east of the Main Gulf Escarpment consists of volcanic flows, breccias, tuffs, lahars, and volcaniclastic conglomerate and sandstone preserved in a complex mosaic of facies belts representing volcaniclastic alluvial-apron to volcanic core and vent positions within the Miocene volcanic arc (Hausback, 1984; Sawlan, 1991).

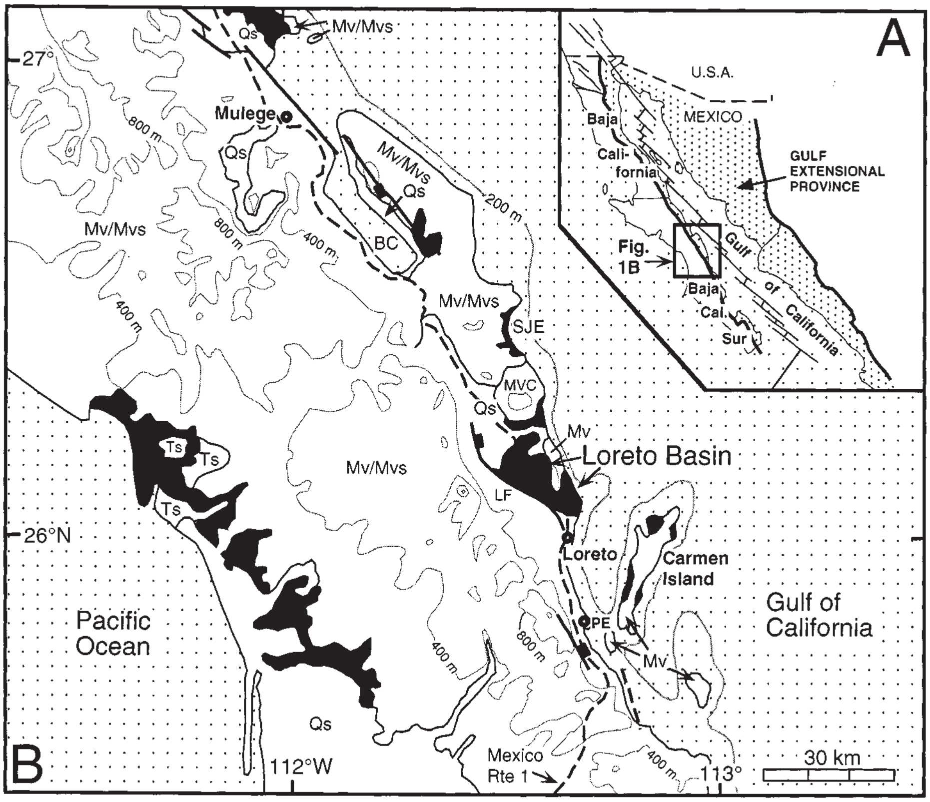

Figure 1. (A) Regional tectonic setting of the Gulf of California and the Baja California peninsula. The Gulf extensional province is a zone of Miocene to Holocene extensional and strike-slip deformation associated with the opening of the Gulf of California. MGE—Main Gulf Escarpment. (B) Simplified geologic map of the Loreto region in Baja California Sur. Black areas represent Pliocene sedimentary rocks. BC—Bahia Concepcion; LF—Loreto fault; MVC—Mencenares volcanic complex (Pliocene–Quaternary); Mv—Miocene volcanic rocks; Mv/Ms—Miocene volcanic and sedimentary rocks; PE—Puerto Escondido; Qs—Quaternary sediments; Ts—Tertiary sedimentary rocks; SJE—San Juanico embayment.

Early to middle Miocene subduction and calc-alkaline volcanism in Baja California were followed by late Miocene regional extension, rifting, and normal faulting along a zone of thick, thermally weakened crust in the Gulf extensional province (Larson, 1972; Hausback, 1984; Stock and Hodges, 1989). In the Loreto area, there is no sedimentary or volcanic record of late Miocene extension. Evidence for this phase of deformation is recorded in an angular unconformity between Miocene volcanic rocks and overlying Pliocene sedimentary rocks (this study), a greater density of faults that cut the older rocks, and the observation that Miocene rocks typically are tilted more steeply to the west than the Pliocene section. The orientation of regional strain changed, from northeast-southwest–directed extension in late Miocene time to east-west extension associated with Pliocene opening of the Gulf of California (Angelier et al., 1981; Stock and Hodges, 1989; Zanchi, 1994; Umhoefer et al., 1997). Pliocene-age structures in the Loreto basin are dominated by north- to north-northeast–striking normal faults and subsidiary northwest-striking strike-slip and oblique-slip faults (Zanchi, 1994; Umhoefer and Stone, 1996).

Pliocene sedimentary rocks exposed discontinuously along the eastern margin of the Baja California peninsula accumulated in transform-rift basins and depressions during opening of the Gulf of California. The Loreto basin (Fig. 2) is the thickest known accumulation of Pliocene deposits exposed on land in eastern Baja California, and thus represents an important record of synrift basin development (McLean, 1988, 1989). The Loreto fault is a large, oblique-slip dextral-normal fault that bounds the southwestern and western margin of the Pliocene Loreto basin (Figs. 1B and 2). The northern termination of the Loreto fault is located west of the late Pliocene Mencenares volcanic complex, and its southern end is buried beneath young alluvium ~5 km north of the town of Loreto (Fig. 1B). Southwest of Loreto, Miocene volcanic rocks dip to the east and are cut by numerous west-dipping normal faults, defining a fault segment that is separated from the Loreto fault by an accommodation zone of relatively low strain. Thus, the Loreto fault does not continue south of Loreto and its length is about 35 km. The late Pliocene Mencenares volcanic center is situated at the northern margin of the Loreto basin (Fig. 1B) and consists of a thick assemblage of andesitic to rhyolitic flows, domes, and pyroclastic rocks and minor basalt flows (Sawlan, 1991; Bigioggero et al., 1995). Its eruptive history overlaps in time (and likely played a role in) the latter half of development of the Pliocene Loreto basin.

LORETO BASIN OVERVIEW

Previous geologic studies of the Loreto basin and surrounding areas have been carried out by numerous workers. During the 1940 Scripps research cruise in the Gulf of California, a brief (1.5 day) reconnaissance survey was made in the area north of Loreto. This included paleontological study of marine molluscan fossils (Durham, 1950) and the first attempt to subdivide the stratigraphy of the Loreto area and correlate formations to Carmen Island (Table 1; Anderson, 1950). McLean (1988, 1989) mapped the structure and stratigraphy of the Loreto area at 1:50 000 scale without subdividing Pliocene strata, and recognized the importance of the Loreto embayment for understanding the evolution of Pliocene structures and basin development. The age of Loreto basin deposits was determined from K-Ar dating of ca. 3.3–1.9 Ma interbedded tuffs (McLean, 1988). Subsequent studies produced a refined understanding of the stratigraphy and structure (Zanchi, 1991, 1994) and paleontology (Piazza and Robba, 1994) of sedimentary rocks in the Loreto basin. The stratigraphic subdivisions proposed by Zanchi (1994) and Piazza and Robba (1994) are mostly corroborated by our work, and are expanded into a formal systematic nomenclature in this paper (Table 1). The volcanology and geochemistry of the Mencenares volcanic center were investigated by Bigioggero et al. (1995). Strata in the northern Loreto basin, exposed on the south flank of the Mencenares volcanic center (Fig. 1B), were examined only in reconnaissance style during our study and are not treated in detail here. Published studies of the Loreto basin by our group (Umhoefer et al., 1994; Dorsey et al., 1995, 1997a, 1997b; Umhoefer and Stone, 1996; Dorsey, 1997; Umhoefer and

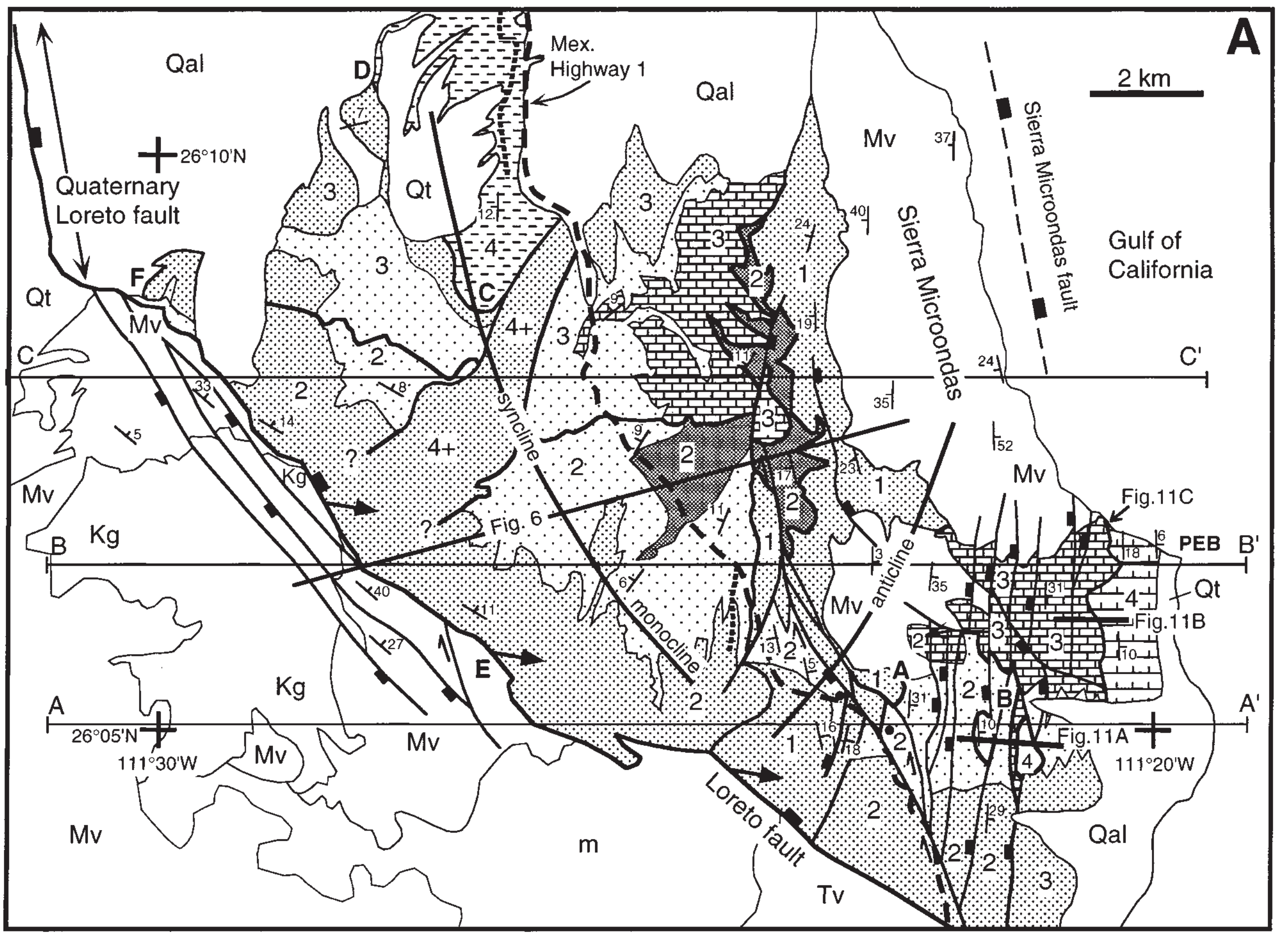

Figure 2. (A) Geologic map of the Loreto basin, showing distribution of pre-Pliocene rocks, Pliocene sedimentary formations and stratigraphic sequences (1–4), and major structures. The central subbasin comprises Pliocene strata located northeast of the Loreto fault, west of the Sierra Microondas, and northwest of the anticline. The southeast subbasin is southeast of the anticline. Figure 7 is a north-south projection of stratigraphic data compiled from the southeast subbasin. PEB—Punta El Bajo (del Tiera Firme). Key for figure is on page 180.

Dorsey, 1997; Falk and Dorsey, 1998) focused on specific aspects of the tectonic, structural, and stratigraphic evolution of the Loreto basin. This paper presents a comprehensive analysis of the entire basin and its history of synbasinal faulting, subsidence, and filling, and interprets that history in terms of controlling factors associated with synbasinal tectonism, eustasy, and sediment input.

The Loreto basin is divided into two subbasins that are separated by a north-northeast–trending anticline at the south end of the Sierra Microondas (Fig. 2). The central subbasin is between the dextral-normal Loreto fault on the southwest and the Sierra Microondas on the east. The southeast subbasin is the area located east and southeast of the anticline, and south of the Sierra Microondas (Fig. 2). A flat pediment (erosion surface) 3–5 km wide is observed to cut little deformed footwall rocks between the Loreto fault and the Main Gulf Escarpment to the west. The pediment is overlain by ~30–50 m of weakly cemented alluvial gravels of probable Pleistocene age that are cut in the north by the northern segment of the Loreto fault (Mayer and Vincent, 1999). The footwall pediment and overlying gravels formed by erosional fault-scarp retreat that probably postdates the main phase of Pliocene basin subsidence and filling. The central and southeastern parts of the Loreto basin have been uplifted and dissected since late Pliocene time, creating excellent exposures of Pliocene sedimentary rocks, while the northern part of the basin has continued subsiding slowly to form a broad alluvial plain in the north (Figs. 1B and 2). This pattern of uplift and subsidence results from fault-controlled uplift in the Sierra Microondas combined with gentle northward tilting and development of a broad, gently north-plunging syncline (Fig. 2).

The history of stratigraphic nomenclature in the Loreto basin is presented in Table 1. The first subdivision of stratigraphy (Anderson, 1950) reflected an attempt to correlate strata of the south-

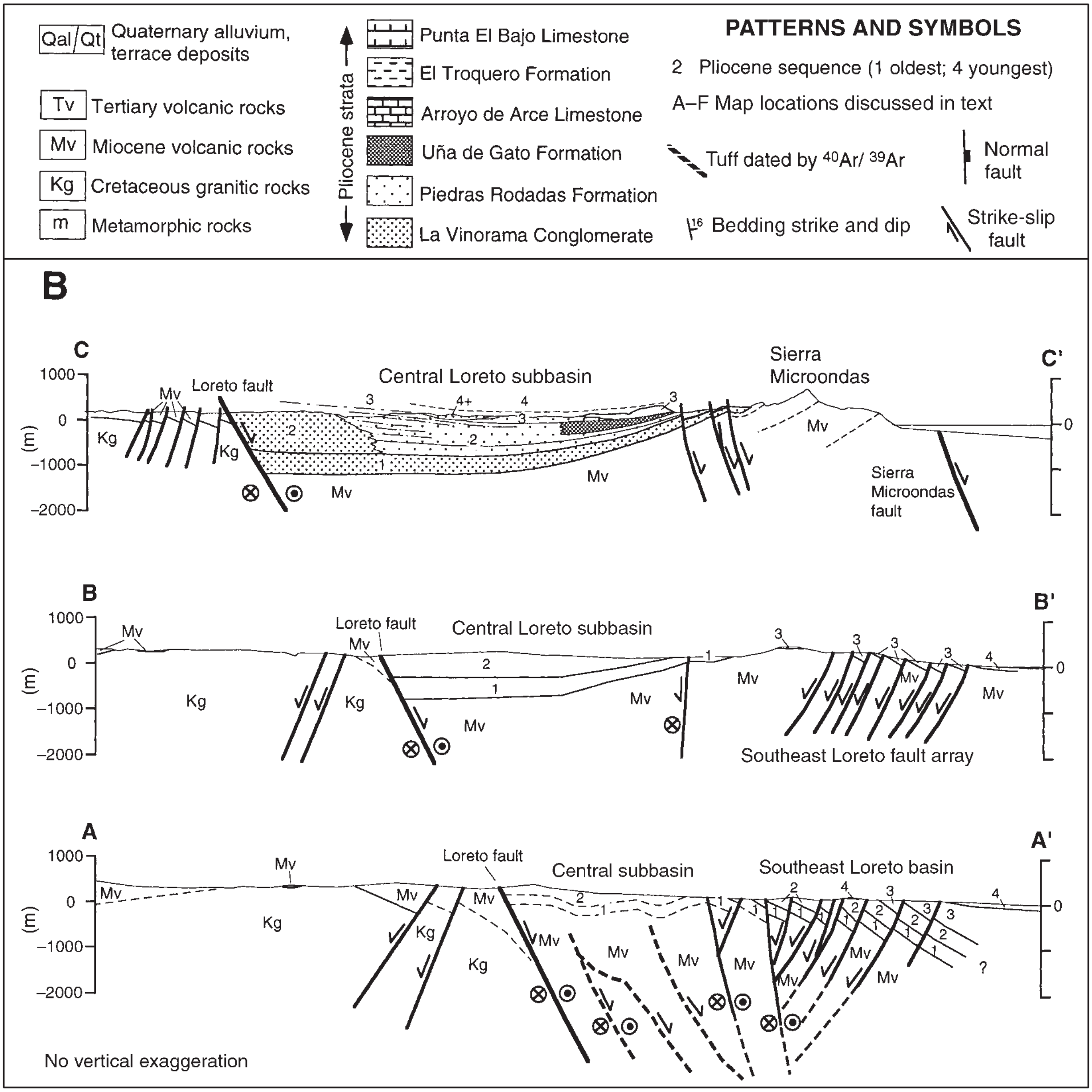

Figure 2. ***(Continued)*****. (B) Geologic serial cross sections through the Loreto basin (no vertical exaggeration).**

TABLE 1. STRATIGRAPHIC NOMENCLATURE FOR THE LORETO BASIN

Anderson (1950)*	Piazza and Robba (1994)	Zanchi (1994)	Dorsey et al. (1995)	This study	Sequence[†]
Carmen and Marquer Formations	San Juan Limestone	San Juan Limestone	Coralgal calcarenite	Punta El Bajo Limestone	4
	El Troquero Volcaniclastics	El Troquero Formation	Gypsiferous mudstone and siltstone	El Troquero Formation	4
San Marcos Formation	Arroyo de Arce Sur Limestone	Canada de Arces Limestone	Conglomeratic bioclastic limestone	Arroyo de Arce Limestone	3
San Marcos Formation	San Antonio Formation	San Antonio Sandstone	Marine to marginal marine sandstone and conglomerate	Piedras Rodadas Formation (upper member)	3
	Uña de Gato Sandstone	Uña de Gato Sandstone	Gypsiferous mudstone and siltstone	Uña de Gato Formation	2
San Marcos Formation	Arroyo de Arce Norte Sandstone Piedras Rodadas Sandstone	Piedras Rodadas Sandstone	Marine to marginal marine sandstone and conglomerate	Piedras Rodadas Formation (lower member)	2
	La Vinorama Conglomerate	La Vinorama Conglomerate	Nonmarine conglomerate and sandstone	La Vinorama Conglomerate (gray member)	1–3
	Cerro Microondas Conglomerate	Cerro Microondas Conglomerate	Nonmarine conglomerate and sandstone	La Vinorama Conglomerate (red member)	1

*Anderson (1950) only pertains to the lower (southern) Arroyo de Arce area.
[†]Sequence designations do not strictly follow the conventions for passive margins (Van Wagoner et al., 1988).

east subbasin to Carmen Island (~20 km southeast of Loreto basin) and San Marcos Island (~130 km northwest of Loreto basin), and did not accurately reflect the complexity of stratal units and their geometrical relationships. A detailed assignment of formation names that describes the lithologies and locations of mappable, distinctive lithosomes in the Loreto basin was proposed by Zanchi (1994) and Piazza and Robba (1994). We have adopted, revised, and expanded that nomenclature into a formal designation of formations and members (Table 1; Fig. 2). An important aspect of organizing the stratigraphy of the Loreto basin has been the recognition of four stratigraphic sequences that can be correlated between different parts of the basin (Fig. 3). The sequences are defined by architectural elements such as unconformities, zones of onlap and downlap, marine flooding surfaces, and parasequence stacking patterns. Sequences have chronostratigraphic significance and are identified by their distinctive features and vertical position in the section, whereas formations in the Loreto basin are strongly time transgressive and their boundaries typically cross time lines at a high angle.

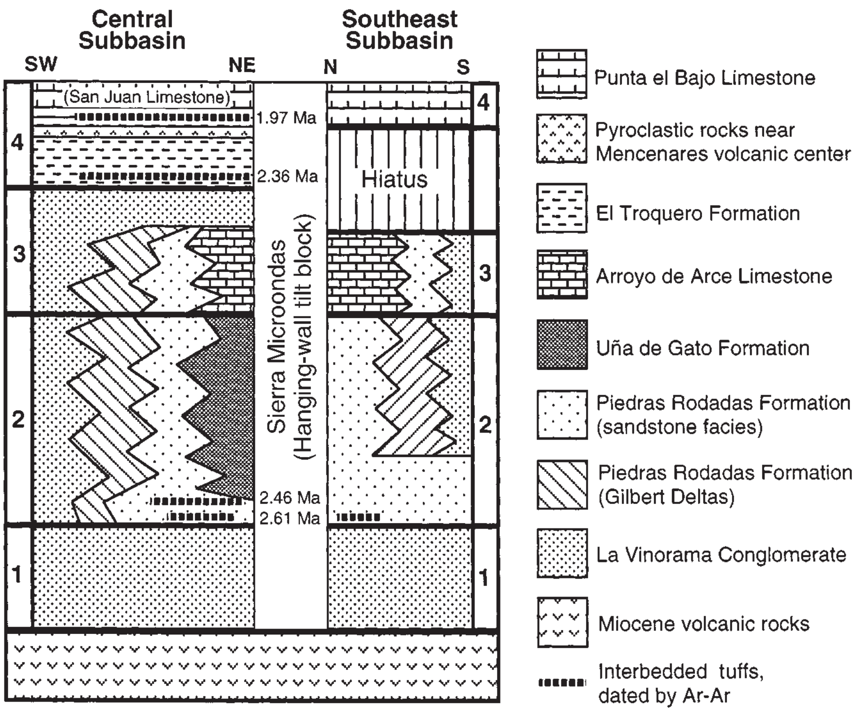

Figure 3. Sequence stratigraphy of the Loreto basin, showing the vertical and lateral distribution of formations within this framework for the central and southeast subbasins.

LITHOSTRATIGRAPHY

Six formations, four dominantly siliciclastic and two dominantly carbonate, compose the major stratigraphic units of the central and southeastern Loreto basin (Figs. 2 and 3; Tables 2

TABLE 2. FORMATION DESCRIPTIONS AND INTERPRETATIONS

Formation	Description	Interpretation
La Vinorama Conglomerate (red member)	Red to reddish-brown hematite-cemented conglomerate. Coarse Variant: Thick-bedded, unstratified, poorly sorted, pebble–cobble–small boulder conglomerate (see Fig. 4A). Clast-supported; max. clasts 40–60 cm diameter, subangular to subrounded. Minor to moderate amount of pebbly sandstone matrix. Beds are ungraded and have tabular to lenticular (channel) geometries. Rare, discontinuous thin beds of pebbly sandstone truncated at base of conglomerate beds. Clasts are andesitic volcanic rocks derived from Miocene volcanic basement. Fine Variant: Trough cross-bedded sandy pebble-cobble conglomerate and minor pebbly sandstone. Clasts subangular to rounded. Weakly developed fining-upward channel-fill intervals 3–10 m thick, sometimes with coarse variant in lower 1–3 m. Some intervals display weak, sheet-like planar to low-angle stratification with no vertical grain-size trends in poorly sorted sandy conglomerate.	Hematite cementation probably produced by postdepositional diagenesis: oxidizing meteoric fluids flushed from uplifted hanging-wall dip slope on eastern side of central basin. Coarse Variant: Deposition by cohesionless, mud-poor debris flows in alluvial fan setting. Thin sand beds record minor surface flow and reworking between constructional events (debris flows). Fine Variant: Deposition by traction currents in gravelly braid-stream system. Some sheet-flood deposition, probably in distal alluvial-fan setting. Association of coarse and fine variants suggests interaction of alluvial fans and braid streams; coarse variant at the base of fining-up intervals represents channel deposition by large boulder-bearing flood flows, probably involving hybrid clast-support mechanisms.
La Vinorama Conglomerate (gray member)	Gray, weakly indurated conglomerate and sandstone, usually covered with slope wash material except in fresh arroyo cuts. Coarse Variant: Poorly sorted to unsorted, structureless to weakly bedded, matrix-supported cobble-boulder conglomerate (see Fig. 4B). Matrix is poorly sorted pebbly sandstone. Clasts are angular to subrounded, maximum size 50 cm to >1 m. Some zones display partial clast support. Rare thin beds of pebbly sandstone truncated at base of conglomerate beds. Fine Variant: Trough cross-bedded sandy pebble conglomerate, pebbly sandstone, and thin (10–30 cm) caliche horizons. Commonly channelized. Fine and coarse variants may be interbedded at 4- to 10-m scale; coarse variant dominates in 2-km-wide belt along Loreto fault (see Fig. 2A).	Lack of cementation results from position within basin that precluded flushing by meteoric waters. Coarse Variant: Deposition by mud-poor debris flows in alluvial-fan setting. Belt along Loreto fault represents steep alluvial fans and debris cones shed off seismically active fault scarp. Fine Variant: Deposition in gravelly and sandy braid stream with periods of overbank soil development. Where occurring in sequence 2 and 3, braid streams formed in intermediate position between alluvial fans (coarse variant) and fan deltas (Piedras Rodadas Formation).
Piedras Rodadas Formation (lower and upper members)	Diverse gravelly and sandy lithofacies described previously by Dorsey et al. (1995) and Falk and Dorsey (1998). Paleontology described by Durham (1950) and Piazza and Robba (1994). Following summary is modified from Dorsey et al. (1995). GD1: Channelized, massive to trough cross-bedded pebble-cobble conglomerate and pebbly sandstone, locally contains mollusk shells. GD2: Pebble-cobble conglomerate and pebbly sandstone with steep primary dips (15°–25°), tabular-bedded to channelized, erosional bed bases, locally inverse and normal grading, shells rare to common (see Fig. 4C). GD3: Thin- to medium-bedded, partially bioturbated sandstone, siltstone, and pebbly sandstone, sharp bases and diffuse tops of beds, some normal grading. GD4: Massive, bioturbated siltstone, sandstone, and/or pebbly sandstone, contains variable molluscan faunal assemblage. GD5: Mollusk-rich shell beds with variable matrix (siliciclastic to calcarenitic sand ± pebbles), and molluscan assemblages ranging from low to high diversity. Pectens, oysters, infaunal bivalves, and gastropods are most abundant; echinoids, barnacles, and calcareous worm tubes are common accessories; rare bryozoans and crabs.	These lithofacies represent the diverse components of Gilbert-type fan deltas (GD) that accumulated downstream of footwall-derived alluvial fans and braid streams (La Vinorama Conglomerate) during sequence 2–3 time. GD1: Topset strata deposited in distributary channels and interdistributary shallow-marine bays. GD2: Foreset strata deposited by gravelly high-density turbidity currents, debris flows, and grain flows on fan-delta slope. GD3: Bottomset strata deposited by distal low-density turbidity currents, with partial biogenic mixing. GD4: Sandy turbidites more distal than GD3, slower sediment accumulation and thus complete homogenization by burrowing organisms. GD5: Hiatal (condensed) shell beds record marine flooding and drowning of fan-delta plain, and nearly complete cessation of detrital input. Episodic alternation of fan-delta progradation and marine flooding probably resulted from episodic subsidence on Loreto fault (Dorsey et al., 1997b).
Uña de Gato Formation	Gypsiferous, thin to very thin bedded, fine- to medium-grained sandstone, siltstone, mudstone, and claystone (see Fig. 4D). Appears massive (and yellow) in weathered slopes, bedded nature only visible in fresh cuts. Bedding geometry varies from planar-tabular to broadly lenticular with shallow scoured bases, with rare meter-scale channel fills. Planar stratification is abundant, some low-angle cross-stratification and ripple lamination. Sole marks (load casts) visible at base of some beds. Gypsum is coarse and fibrous, and occurs in veins to 1.5 cm thick that are both parallel and discordant to bedding (as in Fig. 5C).	Gypsum is secondary and formed by diagenetic oxidation and dissolution of calcite and pyrite, which released Ca^{2+} and S^{2-}. Deposited by dilute sand- and mud-bearing turbidites in the most distal part of footwall-derived fan deltas (Piedras Rodadas Formation). Claystone layers record suspension settling from deltaic fresh-water plumes. Lack of bioturbation indicates conditions unfavorable for benthic faunas (low oxygen and/or low light). Paleodepth is fixed by height of correlative Gilbert-delta foresets (typically 12–30 m) and low slope of bottomset beds, and probably ~20–30 m.
Arroyo de Arce Limestone	Dominant facies is white- to gray-weathering, planar stratified, shelly, sandy and pebbly calcarenite, calcarenitic hash, and calcirudite, carbonate ≥50% (see Fig. 5, A and B). Steep primary dips are seen close to Sierra Microondas. Secondary facies include (1) thin- to thick-bedded, shelly, calcarenitic pebbly sandstone, may display normal grading, planar stratification, and/or ripple cross-stratification; and (2) medium- to thick-bedded shelly conglomerate with hashy sandy calcarenitic matrix, commonly ungraded, normal and inverse grading also seen. Pectens and oysters are most common shell and hash types (Fig. 5B), locally see barnacle hash. Encrusting rhodoliths, bryozoans, and barnacles are common accessories. Shells typically are disarticulated, broken, and current-oriented.	Mixed carbonate and siliciclastic depositional system in which carbonate material consists almost entirely of reworked and transported shells. Carbonates were derived from uplifted hanging-wall dip slope (Sierra Microondas), and were sourced both in contemporaneous mollusk shoals and older eroding limestones. Two main styles of transport and deposition: (1) coarse-grained, mixed-composition debris flows and high- to low-density turbidity currents; and (2) high-energy tidal currents and long-shore currents in shoreface to shallow-shelf setting. Fine-grained variations of both styles are distal equivalents of coarser facies, in a mosaic of current-transported, detrital carbonate, and siliciclastic sediments.
El Troquero Formation	Gypsiferous, bright yellow, massive mudstone and claystone with thin to medium interbeds of marl, siltstone, very fine grained sandstone, and rare siliceous beds (probably diatomite) (see Fig. 5C). Mudrock is dominant, other lithologies minor. Gypsum veins are common to abundant and occur both parallel and discordant to bedding. Diverse assemblage of benthic and planktic forams of outer-shelf to upper-slope affinity recovered from several localities (R. Douglas, 1997, personal commun.). Locally near base may include thin to medium-bedded, hummocky cross-bedded sandstone and (rarely) channelized pebble conglomerate and sandstone.	Gypsum is secondary and formed by same diagenetic processes as described for Uña de Gato Formation. Deposition of clay and silt by suspension settling in very low energy outer-shelf to upper-slope marine setting, far removed from detrital input.
Punta El Bajo Limestone	Massive thick beds of sandy coralgal and molluscan calcarenite with thin to medium interbeds of shelly calcarenitic pebbly sandstone. Coralgal variety is most abundant, mollusk-rich variety is more common near base (Dorsey, 1997). Thick beds of calcarenite-matrix cobble conglomerate are found in fanning-dip section near basal exposure at Punta El Bajo (de Tierra Firme). Mollusk assemblage is similar to that in Arroyo de Arce Limestone. Coralline algae occur both as broken rounded fragments and as partial to whole rhodoliths.	Deposition of carbonate and accessory siliciclastic sediment in a shallow-marine, moderate-energy shelf setting. Unlike Arroyo de Arce Limestone, carbonate was produced in situ. Intermixed siliciclastic sediment represents episodic input by storm events that was thoroughly mixed by burrowing organisms. Interbeds of pebbly sandstone record larger storm events. Cobble conglomerate near base represents rocky shoreline deposits.

and 3). Tables 2 and 3 contain detailed descriptions, interpretations, and other information related to formal definition of the formations. Each formation represents an association of lithofacies that accumulated in related depositional environments. The La Vinorama Conglomerate consists of nonmarine conglomerate and pebbly sandstone and includes facies ranging from thick-bedded, structureless debris-flow facies to trough cross-bedded conglomerate and sandstone of braid stream origin (Fig. 4, A and B; Table 2). The Piedras Rodadas Formation (Fig. 4C) is a variable assemblage of marine to deltaic fossiliferous sandstone and conglomerate that accumulated in Gilbert-type and shelf-type fan deltas derived from the footwall of the Loreto fault (Table 2; Dorsey et al., 1995, 1997b). The Uña de Gato and El Troquero Formations (Figs. 4D and 5C) are gypsiferous fine-grained siliciclastic facies (fine sand to clay) that represent deposition in distal, low-energy marine settings. The Arroyo de Arce Limestone consists of transported carbonate detritus that is mixed with varying amounts of siliciclastic sand and gravel (Fig. 5, A and B). The Punta El Bajo Limestone is dominantly coralline-algal and molluscan carbonate that accumulated, in situ, in a shallow carbonate shelf setting similar to those of the modern Gulf of California (van Andel, 1964; Table 2). The San Juan limestone (Fig. 3) is exposed north of the central subbasin, on the southern flank of the Mencenares volcanic complex (Fig. 1; Zanchi, 1994), and probably is equivalent to the Punta El Bajo Limestone. Additional information about sedimentary lithofacies, depositional processes, and paleoenvironments can be found elsewhere (Dorsey, 1997; Dorsey et al., 1995, 1997a; Falk and Dorsey, 1998).

SEQUENCE STRATIGRAPHY

Reconstructed physical stratigraphic architecture is the basis for defining stratigraphic sequences in the Loreto basin (Figs. 6 and 7). The two-dimensional stratigraphic panels in Figures 6 and 7 were constructed from numerous detailed measured sections that were correlated in conjunction with 1:10 000 scale field mapping. More detailed parts of these panels have been published for the southwestern part of the central subbasin (Fig. 6; Dorsey et al., 1997b) and the marine part of sequence 2 in the southeast subbasin (Fig. 7; Dorsey et al., 1997a). Internal correlations are most reliable in marine sections of the Piedras Rodadas Formation that contain laterally traceable shell beds; this has permitted detailed reconstruction of prefaulting stratal geometries even in the highly faulted southeast subbasin (Fig. 7). The two-dimensional stratigraphic pan-

TABLE 3. FORMATION LOCALITIES AND DEFINITIONS

Formation	Type Locality	Definition	Diagnosis
La Vinorama Conglomerate (red member)	Upper (north) Arroyo de Arce. Northwest quadrant of [2,887-88N; 460-61E]*	Makes up a belt on east side of central basin, west margin of Sierra Microondas. Basal boundary: angular nonconformaity on underlying Miocene volcanic rocks. Upper boundary: base of Piedras Rodadas Formation. Lateral boundaries: not exposed, not important for mapping.	Distinguished from gray member based on well-cemented nature and brown to red color.
La Vinorama Conglomerate (gray member)	1. Cañada El Pozo West 1/2 of [2,883-84N; 459-60E] 2. Arroyos La Vinormama and Las Cuchillas. [2,885-86N; 457-58E]†	Occupies belt along southwest margin of central basin and southern part of south-east basin, local patches in north part of central basin. Basal boundary: not exposed, presumed to be nonconformity on Miocene volcanic rocks. Upper boundary: base of El Troquero Formation. Lateral boundaries: lateral transition north and northeast into marine and Gilbert-delta deposits of Piedras Rodadas Formation (sequence 2–3).	Distinguished from red member based on lack of cementation, poorly consolidated nature, and typical gray color.
Piedras Rodadas Formation (lower and upper members)	2 km along arroyo, northwest of Las Piedras Rodadas. [2,886-87N; 458-60E]	Occupies central axis of central basin and central part of southeast basin. Basal boundary: marine flooding surface at top of La Vinorama Conglomerate (red member). Upper boundary: in central basin = upward gradation into upper (sequence 3) unit of La Vinorama Conglomerate; in southeast basin = low-angle unconformity at base of Arroyo de Arce Limestone. Lateral boundaries: lateral transition to south and southwest into La Vinorama Conglomerate (gray member). Lower member = sequence 2; upper member = sequence 3 (see Fig. 2)	Distinguished from La Vinorama Conglomerate based on common occurrence of marine shells and bioturbated sandstone
Uña de Gato Formation	0.5 km northeast of Mexico Highway 1, north half of [2,888-89N; 458-59E]	Defines a wedge in central basin that thins to the east, also occupies a band west of La Vinorama Conglomerate (red member) on east side of central basin. Basal boundary = deepening-up transition from top of Piedras Rodadas Formation (lower member) or La Vinorama Conglomerate (red member). Upper boundary: gradual transition through sandstone interval into Arroyo de Arce limestone in central basin. Lateral boundaries: lateral transition to the southwest into marine sandstones portion of Piedras Rodadas Formation (lower member).	Distinguished from Piedras Rodadas Formation based on presence of gypsum veins, and thin- to very thin-bedded, well-bedded nature. Distinguished from El Troquero Formation based on location and stratigraphic position.
Arroyo de Arce Limestone	Lower (southern) Arroyo de Arce. On grid line 465E, between 2,884-85N.	Located in northeast part of central basin and northeast part of southeast basin. Basal boundary: in central basin = upward transition through sandstone from Uña de Gato Formation; in southeast basin = low-angle unconformity at top of Piedras Rodadas Formation. Upper boundary: angular unconformity at base of Punta El Bajo Limestone. Lateral boundaries: in central basin, lateral transition westward into siliciclastic sandstone of Piedras Rodadas Formation (upper member, sequence 3); in southeast basin, lateral transition southward into nonmarine facies of La Vinorama Conglomerate (gray member, sequence 3).	Distinguished from Piedras Rodadas Formation based on abundance of transported carbonate material (≥50%). Distinuished form Punta El Bajo Limestone based on transported nature of carbonate and general paucity of rhodoliths.
El Troquero Formation	3 km north-northwest of El Troquero, east side of Arroyo San Antonio, west half of [2,897-98N; 455-56E]	Located in central, axial position in northern part of central basin. Basal boundary: marine flooding surface on top of upper (sequence 3) unit of La Vinorama Conglomerate, central basin. Upper boundary: not analyzed in this study.	Distinguished from Uña de Gato Formation based on location, stratigraphic position, and presence of volcanic tuffs.
Punta El Bajo Limestone	Coastal exposure 0.8 km west-northwest of Punta el Bajo de Tierra Firme, 100–200 m west of [2,887N and 467E].	Exposed in small area in northeast part of southeast basin, best exposed in coastal outcrops. Basal boundary: angular unconformity with underlying Arroyo de Arce, includes basal conglomerate in most localities. Upper boundary: low-angle unconformity at base of Quaternary alluvium deposits.	Distinguished from Arroyo de Arce Limestone based on in situ nature of carbonate and general presence of rhodoliths.

*Brackets indicate 1 km^2 area defined by UTM grids. Northing and easting numbers in kilometers.
†Locality 1 is more easily accessible than locality 2 for which the formation is named.

els (Figs. 6 and 7) were produced by projecting dipping strata into a single vertical plane. In the central subbasin (a gently north plunging syncline), stratigraphy south of the line of section is projected northward into the section, and strata north of the line of section are projected back to the south (Fig. 2). Data used for construction of the southeast subbasin panel (Fig. 7) are unevenly distributed. Most detailed measured sections were collected from sequence 2 and its boundaries (Dorsey et al., 1997a), whereas input for sequences 1, 3, and 4 was based on 1:10 000 field mapping and field estimates of stratigraphic thicknesses.

Composite stratigraphic sections for the central and southeast subbasins illustrate representative vertical trends in lithofacies, grain size, and thickness (Fig. 8). We identify three stratigraphic horizons that correlate between the two subbasins: the base of sequence 2, the top of sequence 2, and shell bed 1 (sb1) in the central subbasin, which correlates to sb4 in the southeast subbasin (Fig. 8). Correlation of the base and top of sequence 2 is straightforward and is supported by detailed mapping of map units and tuff 1 between the two areas. The intermediate correlation, sb1 (central) to sb4 (southeast), is based on inferred ages of shell beds in the southeast subbasin that were determined by correlation to sea-level highstands recorded in the marine oxygen-isotope record (Raymo et al., 1992). Justification for this correlation is presented and discussed in a later section of this paper.

Sequence 1 unconformably overlies Miocene volcanic rocks. It consists entirely of nonmarine conglomerate and pebbly sandstone (lower part of the La Vinorama Conglomerate) that record deposition in alluvial fans and braided streams prior to initiation of marine conditions (Figs. 3, 6, and 7; Table 2). Although there are no thickness data for sequence 1 in the western part of the basin, local stratal geometries and an angular unconformity in the eastern part of the basin (Fig. 6) demonstrate westward tilting toward the Loreto fault during this time. Thus it is possible that sequence 1 is thicker in the deep western part of the basin than is shown in Figures 2B and 6.

The sequence 1–2 boundary is an abrupt marine flooding surface that is laterally traceable in the southeast and southern parts of the central subbasin (Fig. 2). In the southeast subbasin (location A, Fig. 2A), the upper part of sequence 1 consists of 55 m of disorganized pebble- to boulder-clast conglomerate (alluvial-fan debris flows) overlain by 10 m of planar to trough-cross-stratified sandy pebble conglomerate (braid stream facies). The pebble conglomerate is sharply overlain by fine-grained marine deposits at the base of sequence 2. Sequence 2 begins with a 50 cm interval that fines upward from poorly sorted, cal-

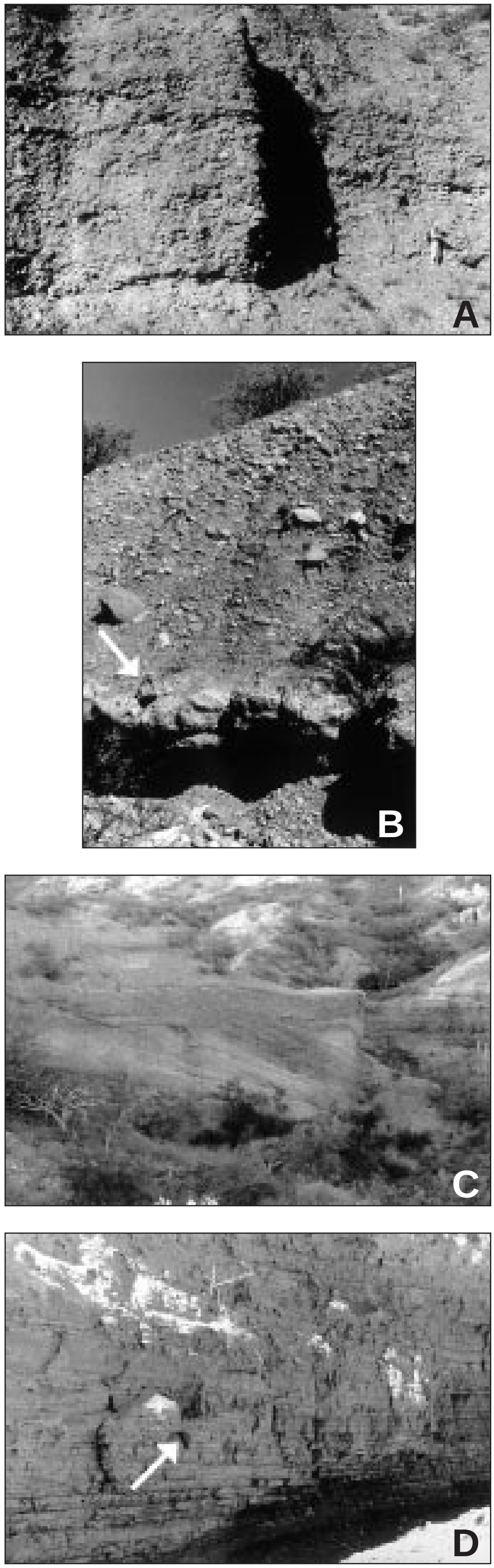

Figure 4. (A) Coarse variant of La Vinorama Conglomerate (red member), showing well-cemented nature of cliff exposure, coarse grain size, and thick massive bedding. (B) Coarse variant of La Vinorama Conglomerate (gray member), showing coarse angular clasts, weak bedding, and weakly cemented erodable nature of deposit. Light-colored ledge at base is one of numerous marine shell beds that cap progradational paracycles in sequence 2 (Fig. 6). Day pack (~45 cm long) is for scale (see arrow). (C) Mixed sand and gravel marine foresets and pebbly fluvial topsets in Gilbert-type fan delta of the Piedras Rodadas Formation. Thickness of exposed foresets is ~7–8 m. (D) Thin-bedded to very thin bedded gypsiferous turbidites comprising fine-grained sandstone, siltstone, and claystone in the Uña de Gato Formation. Gypsum is present as thin veins parallel to bedding. Hammer (left center; see arrow) is 32.5 cm long.

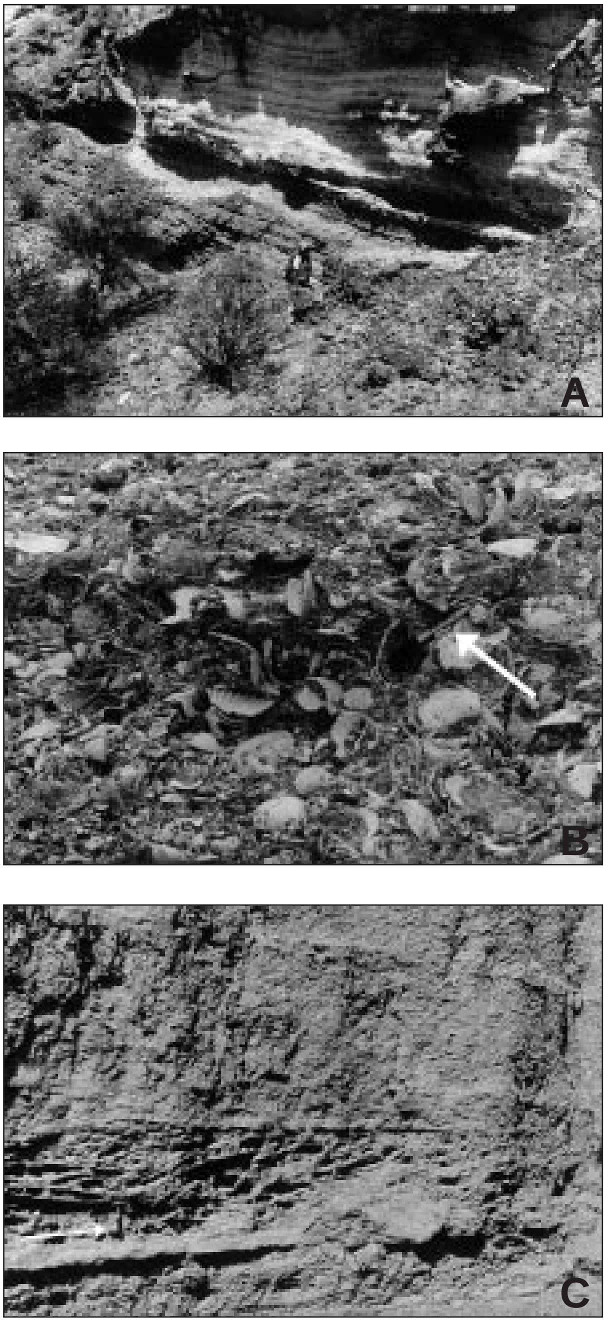

Figure 5. (A) Interstratified bioclastic carbonate and thin-pebble conglomerate in lower few meters of Arroyo de Arce Limestone, southeast subbasin. Lower half of photo consists of siliciclastic conglomerate in uppermost Piedras Rodadas Formation. (B) Transported molluscan shell debris (including pectens, oysters, and encrusting barnacles) in Arroyo de Arce Limestone. Marker pen (right of center; see arrow) is 13.8 cm long. (C) Gypsiferous mudstone, claystone, and marlstone, El Troquero Formation. Note anastomosing structure of gypsum veins on left. Hammer (lower left; see arrow) is 32.5 cm long.

carenitic pebbly sandstone with rare shells and small bivalve molds, into silty fine-grained sandstone with common small bivalves, scattered granules, and a thin concentration of bivalves at the top. Above the bivalve concentration, the section passes upward into massive yellow muddy siltstone with small bivalves and gastropods, which is overlain by thin-bedded bioturbated sandstone beginning ~7 m above the flooding surface.

Sequence 2 is a mosaic of intertonguing footwall-derived nonmarine conglomerate (La Vinorama Conglomerate), marine conglomerate and sandstone (Piedras Rodadas Formation), and thin-bedded fine-grained marine turbidites (Uña de Gato Formation) (Figs. 3, 6, and 7). In the central subbasin, sequence 2 is a strongly westward thickening wedge that coarsens toward the Loreto fault and thins eastward onto the flank of the Sierra Microondas (Fig. 6). In the western half of the central subbasin, deposits of the Piedras Rodadas Formation are organized into ~14 footwall-derived Gilbert-type fan deltas (Table 2) that define an aggradational parasequence stacking geometry (Fig. 6; Dorsey et al., 1995, 1997b). The upper part of sequence 2 reveals a northward progradation of gravel into and along the axis of the basin. Gilbert-type fan deltas comprise parasequences (sensu Van Wagoner et al., 1988) that coarsen upward from fine-grained fossiliferous marine sandstone at the base, through sandy bottomsets and gravely foresets, into channelized conglomerate and interchannel sandstone of the delta-plain setting (topsets) (Table 2). Each parasequence is capped by a 1–2-m-thick marine shell bed that formed during marine hiatus and drowning of the underlying deltaic plain. Fine-grained marine turbidites represent the most distal and fine grained of the footwall-derived siliciclastic facies in the eastward-thinning wedge of the central subbasin. In the southeast subbasin, the lower part of sequence 2 consists of nonmarine conglomerate, conglomeratic and sandy delta-plain facies, and shallow-marine sandstone, and the upper part consists of marine Gilbert-type fan delta deposits similar to those in the central subbasin (Fig. 7; Dorsey et al., 1997a). Sequence 2 in the southeast subbasin contains only four parasequences capped by four laterally continuous shell beds; it is substantially thinner than in the central subbasin, and Gilbert deltas make up only the upper part (Figs. 7 and 8).

The sequence 2–3 boundary varies considerably around the Loreto basin. In the southeast subbasin (location B, Fig. 2A), it is a progressive low-angle unconformity marked by a wedge of growth strata that pinches out updip and is truncated between siliciclastic deposits of sequence 2 and overlying stratified pebbly carbonate of sequence 3 (Fig. 9). A vertical transition is observed within the stratal wedge, from siliciclastic conglomerate and sandstone upward into transported detrital carbonate with minor lithic sand and granules (Fig. 9). This records a rapid change from siliciclastic- to carbonate-dominated deposition and the beginning of major input from the Sierra Microondas during a phase of minor intrabasinal tilting (~6°–8°) and erosion. The continuous appearance of stratigraphy in the

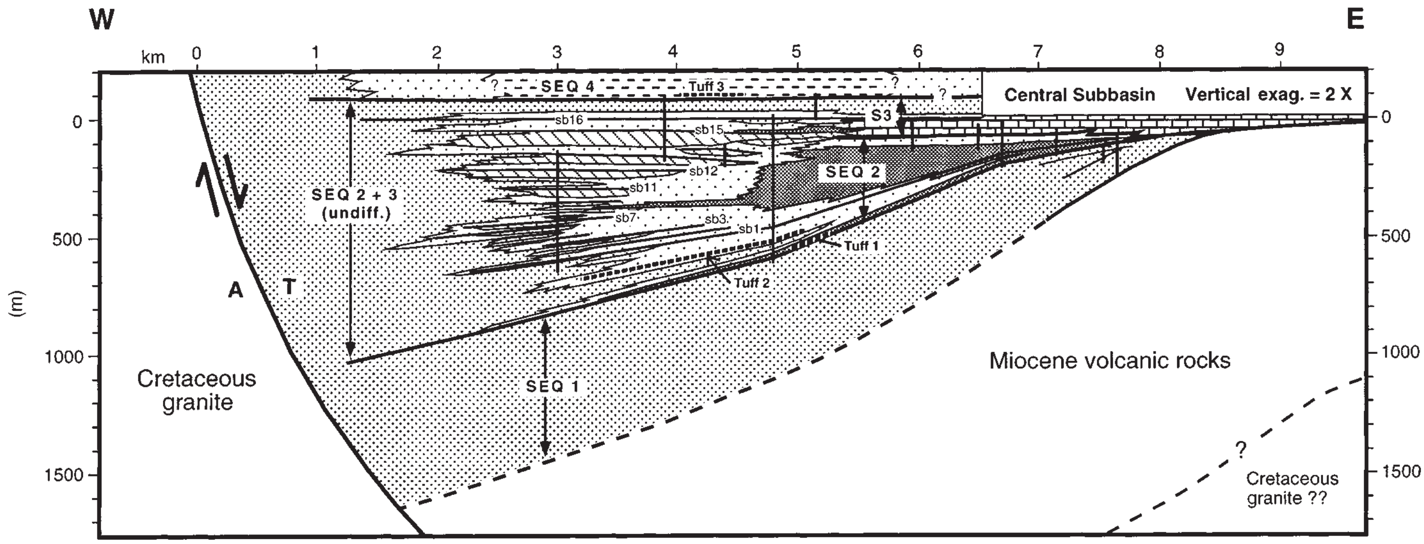

Figure 6. West-east stratigraphic panel across the central subbasin, showing units up through lower part of sequence 4. Patterns represent formations as defined in Figures 2 and 3. sb1–sb16 are marine shell beds that cap progradational Gilbert-delta paracycles in footwall-derived strata of sequences 2 and 3. Vertical lines represent measured sections that were correlated in detailed field mapping. Note strong westward thickening of sequence 2, which thins and pinches out eastward onto west flank of Sierra Microondas. See Figure 2 for location of panel.

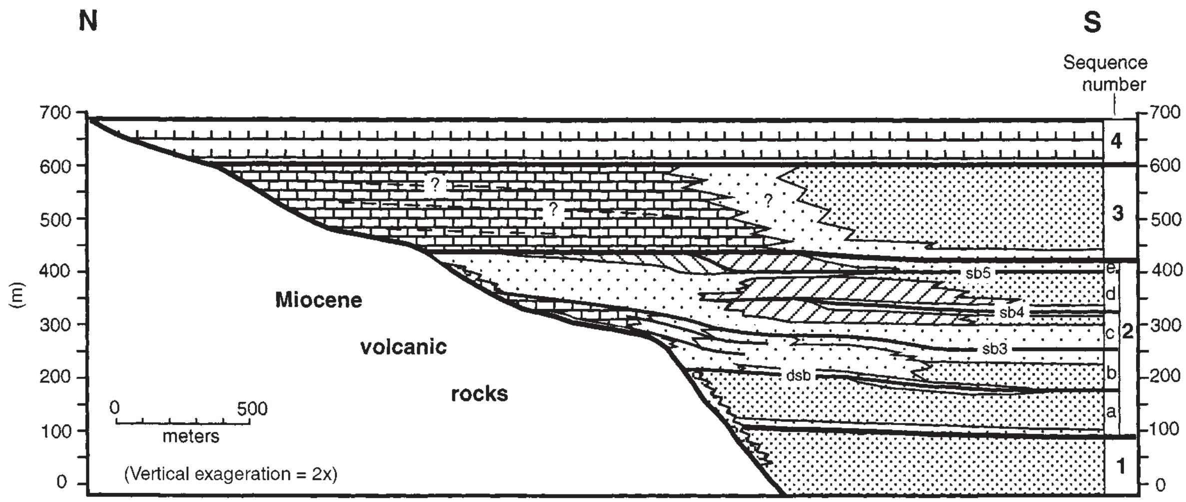

Figure 7. North-south stratigraphic panel for the southeast subbasin (Fig. 2). Panel is a composite of detailed mapping and measured sections (sequences 1 and 2; Dorsey et al., 1997a) and reconnaissance mapping and stratigraphy (sequences 3 and 4; our unpublished mapping). Dsb—double shell bed; sb3–5—other laterally continuous shell beds that define paracycles in southeast subbasin. Shell beds 1 and 2 are between dsb and sb3 on the northern margin of the panel, and are not significant in the stratigraphic architecture at this scale.

downdip part of the growth wedge (Fig. 9) indicates that little or no time is missing at this contact. The sequence 2–3 contact in the eastern half of the central subbasin is a thin progradational transition, from fine-grained siliciclastic sandstone derived from the footwall of the Loreto fault into strongly progradational and downlapping Gilbert-type fan deltas composed of transported gravelly bioclastic carbonate derived from the Sierra Microondas to the east (Fig. 5C). East of there, bioclastic carbonate of sequence 3 unconformably overlies sequence 1 conglomerate and Miocene volcanic rocks on the west flank of the Sierra Microondas (Fig. 6). In the western half of the central subbasin, where no easterly derived detrital carbonate accumulated, the sequence 2–3 boundary coincides with a parasequence boundary.

Sequence 3 (Arroyo de Arce Limestone; Fig. 5, C–E) is characterized by abundance of transported pebbly and sandy bioclastic carbonate that makes up several parasequences. In the central subbasin, sequence 3 has approximately uniform east-west thickness, in contrast with the strongly westward-thickening geometry of sequence 2 (Fig. 6). Here, it consists of coarse-grained shell-rich bioclastic limestone mixed

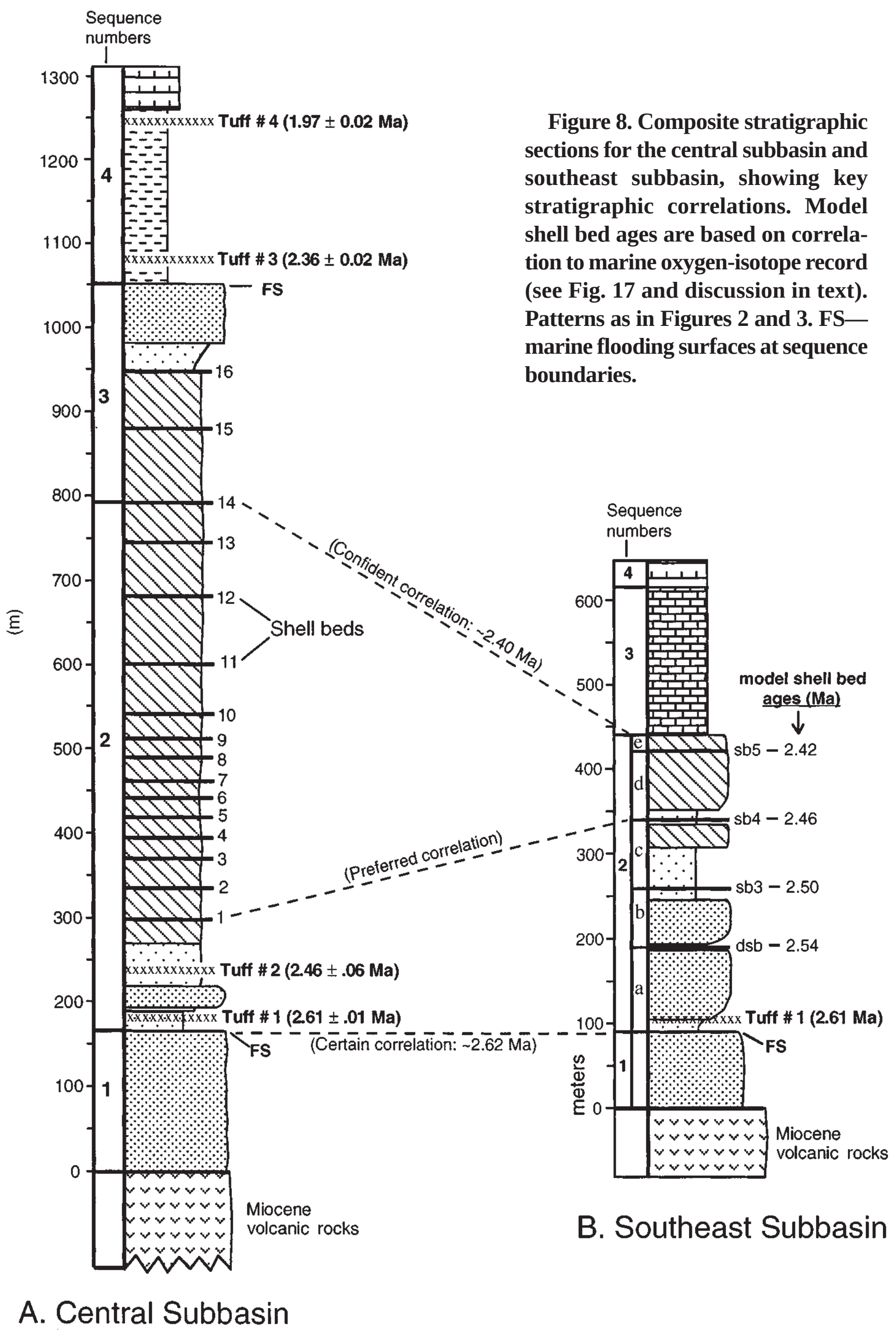

Figure 8. Composite stratigraphic sections for the central subbasin and southeast subbasin, showing key stratigraphic correlations. Model shell bed ages are based on correlation to marine oxygen-isotope record (see Fig. 17 and discussion in text). Patterns as in Figures 2 and 3. FS—marine flooding surfaces at sequence boundaries.

with lithic sandstone and conglomerate in an association of distinctive foreset and bottomset stratal geometries that define large, easterly derived marine Gilbert-type fan deltas (Dorsey and Kidwell, 1999).

These carbonate fan deltas interfinger with deltaic and marine sandstone of the Piedras Rodadas Formation to the west, which in turn pass westward into nonmarine conglomerate of the La Vinorama Conglomerate close to the Loreto fault. The upper part of sequence 3 reveals a coarsening- and shallowing-upward gradational transition into nonmarine conglomerate that extends across the entire width of the central subbasin (Figs. 2 and 6). In the southeast subbasin, sequence 3 bioclastic carbonate (Arroyo de Arce Formation) onlaps onto the southern margin of the Sierra Microondas and passes laterally to the south into footwall-derived conglomerate and sandstone (Figs. 2 and 7). Field mapping in the southeast subbasin indicates the presence of three coarsening-up paracycles that may correlate to paracycles in the eastern part of the central subbasin, but that correlation is tentative and remains untested.

The sequence 3–4 boundary is an abrupt marine flooding surface in the central subbasin and an angular unconformity in the southeast subbasin (Figs. 3, 6, and 10). At location C (central subbasin, Fig. 2A), poorly sorted nonmarine conglomerate in the upper part of sequence 3 is sharply overlain by ~4 m of muddy, very fine grained sandstone with abundant infaunal bivalves indicative of a low-energy marine shelf setting. The fossiliferous sandstone passes upward into yellow-ochre clayey siltstone and mudstone of the El Troquero Formation (distal outer shelf). At location D (Fig. 2A), the marine flooding surface is overlain by a complex assemblage, about 6–8 m thick, of shallow-marine, thin-bedded sandstone, mudstone, and channelized sandstone and sandy pebble conglomerate. That passes upsection over ~2–4 m into thin- to very thin bedded sandstone-mudstone turbidites and interbedded gypsiferous mudstone. Two short cross sections in the southeast subbasin reveal the erosional angular unconformity between moderately dipping strata of sequences 2 and 3 and shallowly dipping limestone and conglomerate of sequence 4 (Fig. 10, A and B). The angular discordance between rocks below and above the unconformity is 20°–25°. A fanning-dip section exposed on the coast (Fig. 10C) records syndepositional tilting that produced this unconformity (Dorsey, 1997).

Sequence 4 in the central subbasin contains ~200 m of distal marine mudstone and claystone (El Troquero Formation) that is interbedded with pyroclastic tuffs and tuff breccias that thicken rapidly northward toward the Mencenares volcanic center (Table 2; Fig. 8A; Bigioggero et al., 1995). On the southern flanks of the Mencenares complex (Fig. 1B), the upper El Troquero Formation and interbedded thick tuffs are overlain by the shallow-marine San Juan Limestone. The San Juan Limestone is defined in the north-central subbasin, and it contains complexly channelized, interbedded, and intermixed volcanic tuffs and flows derived from the Mencenares center (Zanchi, 1994; Bigioggero et al., 1995). In the southeast subbasin, sequence 4 consists of shallow-dipping mollusk- and rhodolith-bearing carbonate and two or three patches of conglomerate in the central part of the southeast subbasin that unconformably overlie more steeply dipping strata of sequences 2 and 3 (Figs. 2 and 10B; Table 2; Dorsey, 1997). On the basis of lithologic correlation, we infer that the El

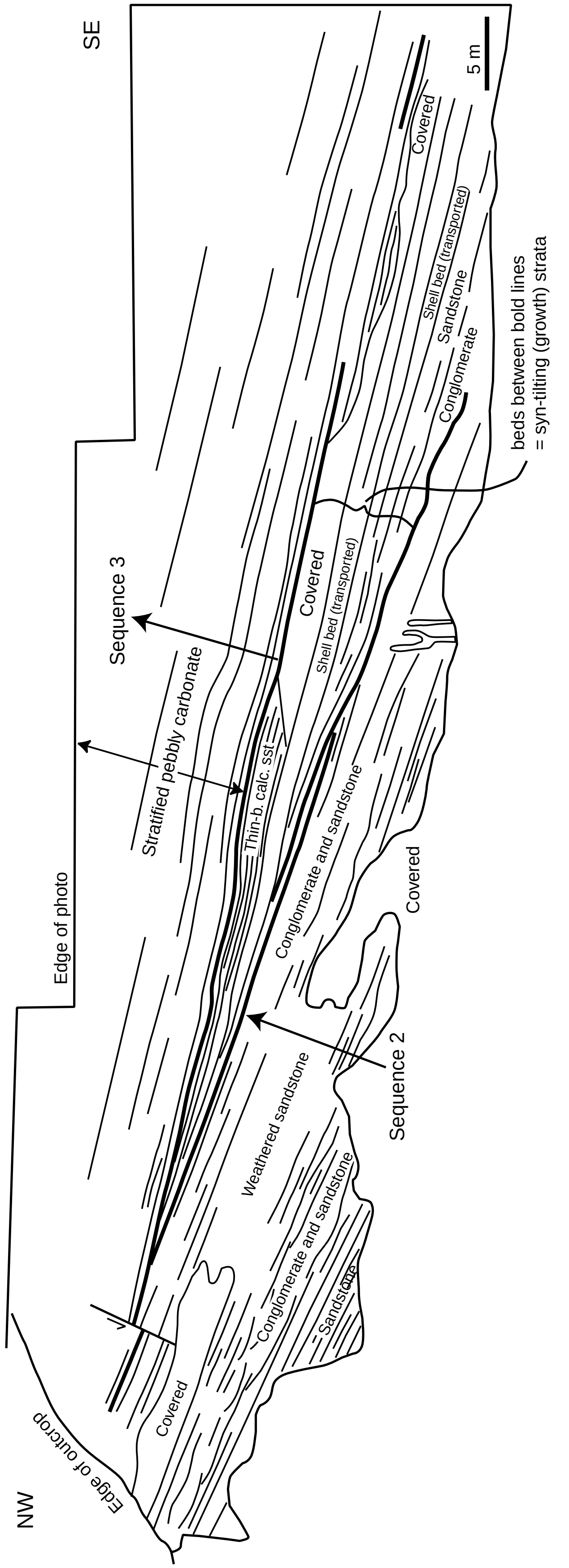

Figure 9. Line drawing from photomosaic showing wedge of growth strata and low-angle unconformity at sequence 2–3 boundary, location B in the southeast subbasin (Fig. 2). Beds beneath the wedge dip ~20° east, and beds above it dip ~12°–13° east. Beds within growth wedge show persistent updip truncations against base of progressively younger beds, recording syndepositional tilting during development of the sequence boundary.

Troquero Formation in the central subbasin (lower part of sequence 4) is equivalent to the erosional unconformity between sequences 3 and 4 in the southeast subbasin (Fig. 3). Independent age data are not available for testing this correlation.

PALEOCURRENT DATA

Paleocurrent data for sequences 1–3 were collected from cross-bedding, clast imbrications, and restored primary dips of Gilbert-delta foresets in different parts of the Loreto basin (Fig. 11). Data for sequence 1 (conglomerate clast imbrications) were collected in the eastern part of the central subbasin and the northwestern part of the southeast subbasin, and reveal consistent transport toward the west (Figs. 2 and 11A). Sequence 2 paleocurrent indicators from the south-central subbasin (conglomerate clast imbrications and restored foreset dip directions) record transport toward the north and north-northeast with little scatter (Fig. 11B). Paleocurrent data from the south-central subbasin show the greatest amount of variation within individual Gilbert-delta parasequences, with relatively little variation between parasequences (Falk, 1996). The only significant trend in these data is that Gilbert deltas located in the very southernmost part of the central subbasin show an average paleocurrent direction of 353°, whereas Gilbert deltas located farther to the northwest yield average transport directions of 023° (north-northeast) (Fig. 2). In the southeast subbasin, sequence 2 paleocurrents reveal a greater amount of variation, with transport directions toward the north, northeast, east-southeast, and a minor component toward the northwest (Fig. 11C). East-southeast–directed data were collected from near the top of sequence 2 and from limited localities of sequence 3 in the southeast subbasin. Paleocurrent data for sequence 3 were collected primarily in the eastern part of the central subbasin (Fig. 2), from clast imbrications, trough cross-bedding, and linear features such as parting lineations and trough axes. The data for sequence 3 show a dominant mode toward the northwest with substantial variation and significant smaller modes in the northeast quadrant (Fig. 11D).

SUBSIDENCE ANALYSIS

Central Subbasin

Curves for total and tectonic subsidence in the central subbasin (Fig. 12) were constructed using sedimentary thicknesses, lithologies, paleodepths, and ages of interbedded tuffs (Umhoefer et al., 1994) in the composite stratigraphic section of the central subbasin (Fig. 8A). Sequence 1 is undated,

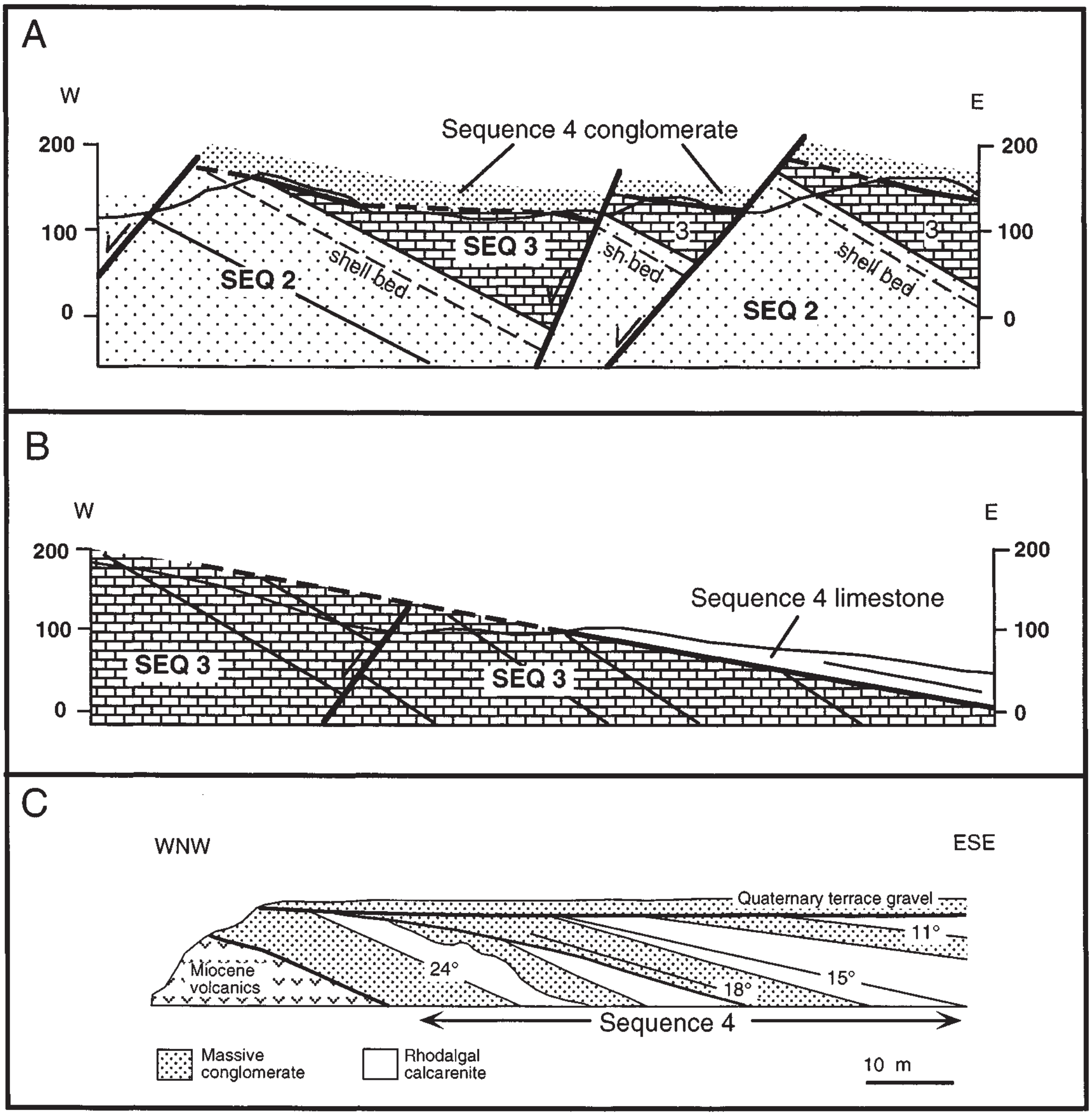

Figure 10. Three cross sections showing sequence 3–4 boundary in the southeast subbasin. (A) Angular unconformity overlain by sequence 4 conglomerate. (B) Angular unconformity overlain by sequence 4 limestone. (C) Fanning-dip section showing progressive decrease in eastward bedding dip from uppermost sequence 3 into lower sequence 4 (modified from Dorsey, 1997). Dip decrease continues eastward into dips of ~3°–6° at Punta El Bajo. Section C records tilting phase that produced angular unconformity in A and B. Location of sections is shown in Figure 2.

but because the sequence 1–2 boundary is nonerosive it is likely that most or all of sequence 1 is Pliocene in age. A subsidence curve for this section first appeared in Dorsey et al. (1995). We have subsequently refined the curve by adding new information about water depth in the lower part of sequence 4 (125 ± 25 m; R. Douglas, 1997, written commun.), computing the tectonic component of subsidence, adding uncertainties for possible variations in eustatic sea level, and expanding the very rapid part of the curve (2.46–2.36 Ma) with an interpretation based on constraints from internal stratigraphy (Fig. 12). Standard numerical techniques for sediment decompaction and backstripping were used in this analysis (e.g., Steckler and Watts, 1978; Angevine et al., 1990). Tectonic subsidence is calculated assuming local isostatic response to loading, and represents subsidence that would occur in the absence of a sedimentary load. Sea level is generally believed to have fluctuated by ~80–120 m during middle to late Pliocene time (e.g., Raymo et al., 1992). This introduces uncertainties in total and tectonic subsidence that range from ± 40 m to ± 60 m and are represented by an error envelope in Figure 12.

Figure 12A reveals a strongly episodic history in which relatively slow or moderate subsidence (~0.4 mm/yr) was punctuated by one short burst of extremely rapid subsidence (8 mm/yr) bracketed between tuffs 2 and 3. Most of the thickness of stratigraphy in the central subbasin (>800 m; Fig. 8A) accumulated during this short time interval (~100 k.y.). This behavior is predicted for strike-slip–related basins (Christie-Blick and Biddle, 1985; Pitman and Andrews, 1985; Johnson et al., 1983), but rarely is it this tightly constrained by high-precision age dating. The rate of tectonic subsidence following the very rapid pulse is basically zero.

Southeast Subbasin

We calculate subsidence rates for sequence 2 in the southeast subbasin using stratal thicknesses and ages shown in Figure 8. The water depth remained close to sea level during this interval, and therefore the subsidence rate is approximately equal to the net rate of sediment accumulation. Bracketing ages in this section are provided by tuff 1 (2.61 Ma) near the base of sequence 2 and by the inferred age of the sequence 2–3 contact, which is well correlated to the central subbasin where an age of 2.40 Ma is assigned by interpolation between tuffs 2 and 3 (Fig. 8). These age and thickness constraints yield a subsidence rate of ~1.5 mm/yr for sequence 2 in the southeast subbasin.

STRUCTURAL GEOLOGY

The Loreto basin is bounded on the southwest and west by the Loreto fault (Fig. 2A), which was the primary structure responsible for basin subsidence. In most of the map area the fault strikes northwest and separates Miocene volcanic rocks, Cretaceous granite, and Mesozoic(?) metavolcanic rocks of the footwall from Pliocene strata and underlying Miocene volcanic rocks of the hanging wall. A major northeast-trending anticline separates a broad open syncline in the central subbasin from faulted, east-dipping rocks in the southeast subbasin (Fig. 2A). The southeast subbasin contains a dense array of normal and dextral-normal faults, the southeast fault array (Fig. 2; Umhoefer and Stone, 1996). The southeast fault array is thought to merge to the south with the Loreto fault, but faults are poorly exposed in the area where they would merge. The Sierra Microondas fault is a north-striking, down-to-the-east normal fault located near the coast on the east side of the Sierra Microondas (Fig. 2A).

Loreto Fault and Central Subbasin

The Loreto fault is a major fault with a dogleg shape (Figs. 1 and 2). The southern segment of the fault is well defined for ~20 km, starting near the Baja highway about 5 km north of Loreto (south edge of the geologic map, Fig. 2A) and continuing northwest to the dog-leg bend where it joins the Quaternary northern segment. The southern segment strikes northwest and includes a 1–2-km-wide zone of antithetic normal and dextral-normal faults in the footwall. There is no evidence for Quaternary or Holocene faulting along the southern fault segment. In contrast, the northern segment has ~4–7-m-high fault scarps for its entire 12 km length (Mayer and Vincent, 1999). There is no sign of the Loreto fault more than ~12 km north of the dogleg bend. Although there are no Pliocene strata exposed immediately adjacent to the northern part of the Loreto fault, we interpret that the northern part was active in Pliocene time based on its lateral continuity with the southern fault and the presence of Pliocene strata a few kilometers to the east (Fig. 2A).

In detail, the southern Loreto fault has many small bends and jogs. The fault is well exposed in five locations and is best exposed where it crosses Arroyo El Leon (location E, Fig. 2A). At one place the fault has two overlapping strands for ~300 m with a step between them. In another area, the fault forms a small, northwest-facing graben with high-angle boundaries. Where Arroyo El Salto crosses the fault (location F, Fig. 2A), the fault is a complex, ~2-km- long zone. There, the fault splays and exposes a small patch of marine strata that appears to form a buttress unconformity against Miocene volcanic rocks within a fault wedge. This suggests that the fault had additional steps when it was active, which would allow local buttress of Pliocene strata against footwall rocks. Where well exposed, the Loreto fault dips ~50°–70° to the northeast. It is a ~0.3–1-m-wide zone of clay gouge juxtaposed against hanging-wall conglomerate. The gouge is against a variably thick zone of fault breccia that consists of centimeter-scale faulted and fractured footwall rocks and is typically 1–2 m thick. The fault breccia grades abruptly into an ~5–10-m-thick zone of decimeter-scale faults and fractures of the footwall rocks. Conglomerate in the hanging wall has few faults or fractures and shows local coarsening and increasing clast angularity toward the fault.

A large, open syncline occupies the central subbasin between the Loreto fault and the Sierra

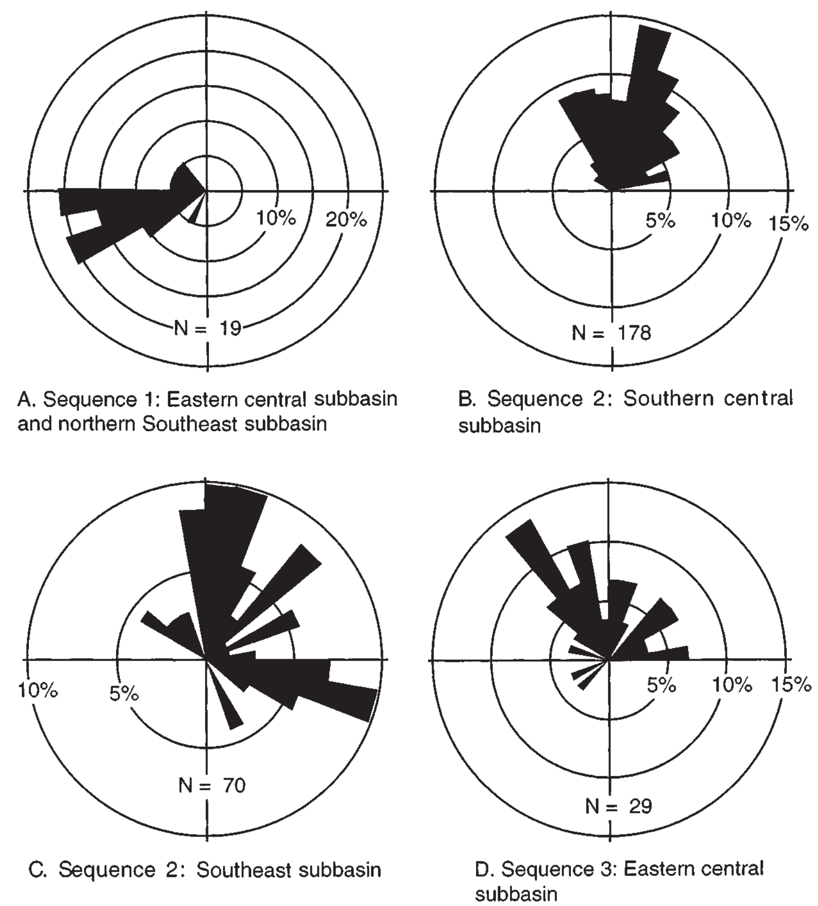

Figure 11. Paleocurrent data from the Loreto basin plotted as rose diagrams. Number of data points (N), percentage contours, location, and stratigraphic sequence are indicated for each diagram.

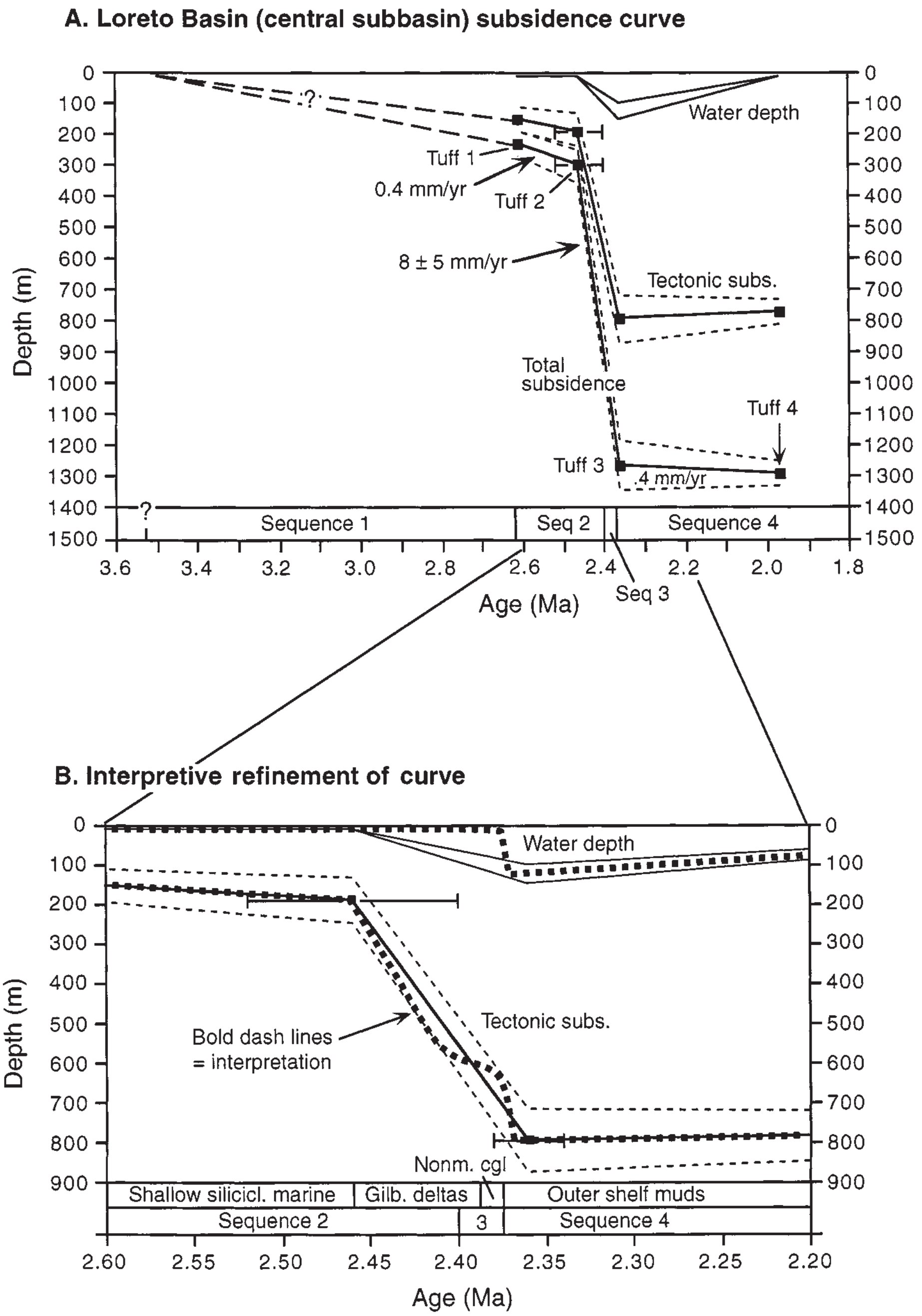

Figure 12. Decompacted subsidence curve (A), and interpretive refinement (B) for the central subbasin. Data for thickness, lithology, and age are illustrated in Figure 8A. Thin dashed lines represent uncertainties related to possible eustatic sea-level fluctuations. See text for discussion.

Microondas structural block (Fig. 2) and is best defined in sequence 2. The syncline plunges gently to the north-northwest (346°) and merges southward into a northwest-trending monocline. The monocline is about 2.5 km long and 300–500 m wide, and locally tilts Pliocene strata as much as 36° to the northeast. A moderately closed anticline and complex growth syncline are exposed just west of the Sierra Microondas. These folds are spatially related to moderate-size dextral-normal faults that extend along the Baja Highway and along the southwest side of the Sierra Microondas. A syncline in this area shows evidence for syndepositional folding of Gilbert-type fan deltas in the lower part of sequence 3.

Southeast Fault Array

The fault array in the southeast subbasin was described in detail elsewhere (Umhoefer and Stone, 1996). It is an anastomosing array of dominantly north-striking, west-dipping normal faults and northwest-striking dextral-normal faults. A minority of the faults is north-northeast–striking sinistral-normal faults. The southeast fault array appears to diverge from the Loreto fault from the south as a series of antithetic faults (Fig. 2). The dextral-normal faults are primarily found in a narrow zone along the Baja Highway and the southwest margin of the Sierra Microondas (Fig. 2). The rest of the fault array consists of normal faults and a few oblique-slip transfer faults. Individual faults show tens to a few hundred meters of offset, well defined by offset marker beds. Normal faults have tilted the Pliocene strata 30°–40° to the east within the southeast basin, and they record ~35% extension. The west-dipping faults in the eastern part of the southeast fault array have been mapped northward into Miocene volcanic rocks, where they are difficult to detect. Here they merge northward with a complex coastal fault domain (accommodation zone) ~1.5 km wide, where the coastline bends to the north and parallels the Sierra Microondas fault (Figs. 2A and 13H).

North of the southeast fault array, the east side of the Sierra Microondas along the coast has many small faults cutting west-dipping Miocene volcanic rocks that are dominated by east-dipping normal faults (Fig. 2; north domain of Sierra Microondas fault, Fig. 13G). The eastern side of the Sierra Microondas is topographically steep and rises rapidly from the beach to more than 600 m elevation in 1–1.5 km. We infer the presence of a large, active down-to-the-east normal fault located ~1–2 km offshore from the Sierra Microondas, which we call the Sierra Microondas fault. In addition, Nava-Sanchez (1997) mapped a down-to-the-east normal fault about 1–1.5 km offshore at the northern end of the Sierra Microondas in Holocene sediments from single channel seismic data. This offshore fault coincides closely with the proposed Sierra Microondas fault. We interpret the transitional domain of complex faulting, which is located between the west-dipping normal faults of the southeast fault array and the east-dipping Sierra Microondas fault, to be a local accommodation zone. It appears that the southern part of the Sierra Microondas fault bends eastward into an east-west fault just north of Punta El Bajo (Fig. 2), because uplifted marine terraces are preserved at the point and west of it (Mayer and Vincent, 1999).

The angular unconformity at the base of sequence 4 in the southeast subbasin (Fig. 10, A and B) provides further evidence that the south-

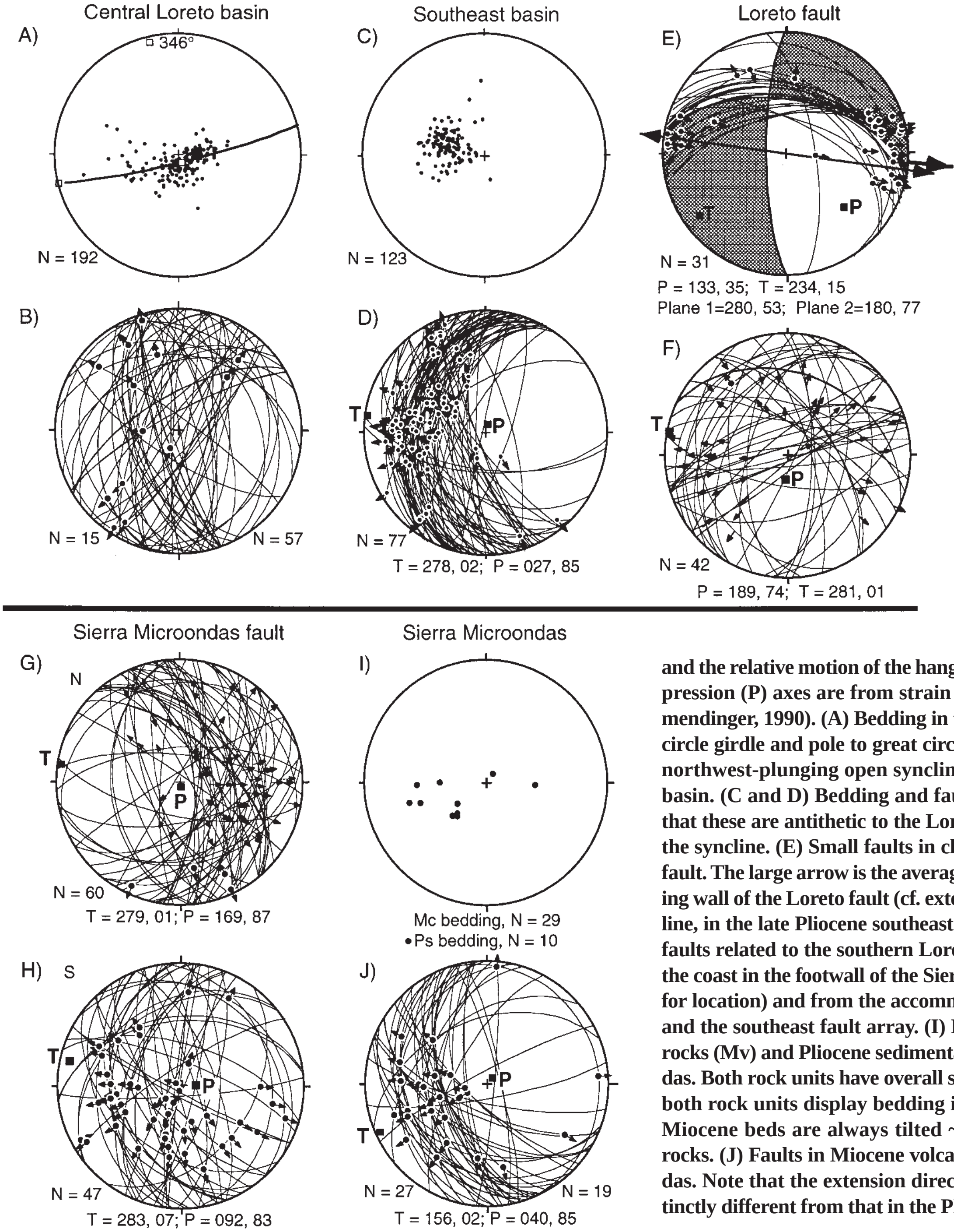

Figure 13. Equal-area plots of structural data from the Loreto basin. With the exceptions noted here, dots are poles to bedding; great circles are fault planes; ball and arrow symbols on great circles are the trend and plunge of striae and the relative motion of the hanging wall. Extension (T) and compression (P) axes are from strain analysis (after Marrett and Allmendinger, 1990). (A) Bedding in the central subbasin with a great circle girdle and pole to great circle representing the gently north-northwest-plunging open syncline. (B) Faults in the central subbasin. (C and D) Bedding and faults in the southeast basin. Note that these are antithetic to the Loreto fault and the eastern limb of the syncline. (E) Small faults in clay gouge in the southern Loreto fault. The large arrow is the average azimuth of motion of the hanging wall of the Loreto fault (cf. extension direction, double-arrowed line, in the late Pliocene southeast fault array in D). (F) Secondary faults related to the southern Loreto fault. (G and H) Faults along the coast in the footwall of the Sierra Microondas fault (see Fig. 2A for location) and from the accommodation zone between that fault and the southeast fault array. (I) Bedding in the Miocene volcanic rocks (Mv) and Pliocene sedimentary strata in the Sierra Microondas. Both rock units have overall similar amounts of tilt, but where both rock units display bedding in close proximity to each other, Miocene beds are always tilted ~5°–10° more than the Pliocene rocks. (J) Faults in Miocene volcanic rocks in the Sierra Microondas. Note that the extension direction is northeast-southwest, distinctly different from that in the Pliocene faults.

east fault array and faults on the west side of the Sierra Microondas were active prior to and during sequence 4 time. A fanning-dip section at Punta El Bajo (Fig. 10C) shows that eastward tilting, which produced the angular unconformity, occurred by slip on west-dipping normal faults during deposition of rocky shoreline and shallow-marine sediments in the lower part of sequence 4 (Dorsey, 1997). This phase of syndepositional tilting was produced by faulting in the southeast fault array early in sequence 4 time. The age of sequence 4 in the central subbasin is 2.36–2.0 Ma. Evidence from the base of sequence 3 (Fig. 9) suggests that deformation in the southeast fault array began early in sequence 3 time, ca. 2.4 Ma. Based on extrapolation of ages from the central subbasin, this faulting episode was mostly completed before 2.0 Ma, with a few small faults continuing to slip and cut sequence 4 strata. There is no sign that the onshore southeast fault array is active today. Thus, we interpret that sometime after 2.0 Ma, the southeast fault array became inactive, but the Sierra Microondas fault continued to slip until the present day.

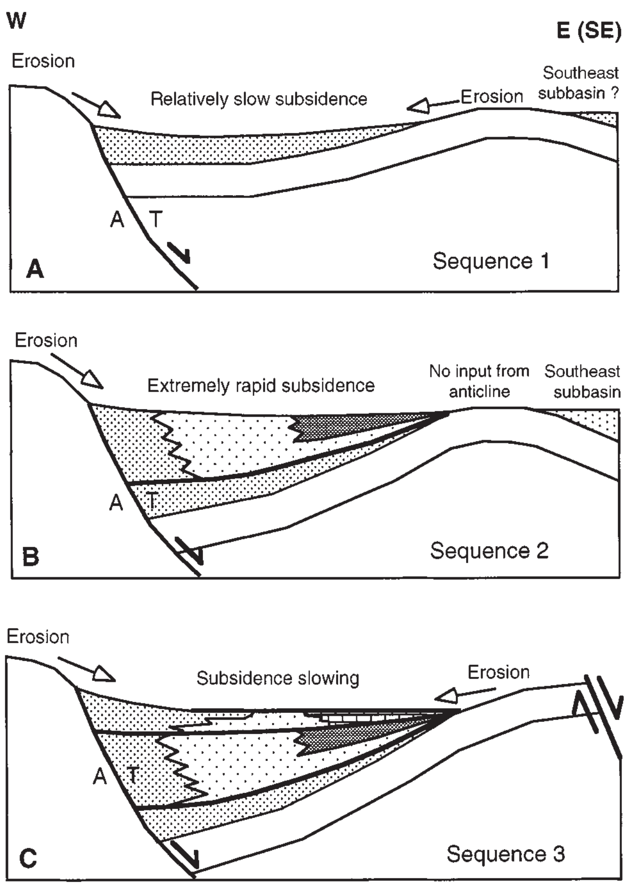

Figure 14. Interpretive three-stage evolution of central subbasin (cross-section view), in which basin subsidence is controlled by growth of hanging-wall collapse syncline (sequence 1 and 2), followed by slowing of slip on Loreto fault, initiation of coastal fault in the east, and uplift and erosion of hanging-wall tilt block (sequence 3). Note oblique nature of cross section, which results from oblique nature of controlling structures: cross-section view is west-east for central subbasin and northwest-southeast for southeast subbasin (see Fig. 2A).

Kinematic Analysis

The map distribution and kinematics of faults in and along the margin of the Loreto basin indicate that they were active in the same strain regime and acted as an integrated system of normal and oblique-slip faulting (Fig. 13). Analysis of the Loreto fault shows down-to-the-east motion, which demonstrates that the fault drove basin subsidence (Fig. 13, E and F). All faults that cut the Loreto basin have a similar extension direction. Dominantly normal faults of the southeast fault array indicate extension to 278°, Sierra Microondas faults record extension to 279°, and the accommodation zone between them shows extension to 283° (Fig. 13, D, G, and H). Fault striae on secondary faults related to the Loreto fault, along its southeastern part, yield a similar extension direction (281°, Fig. 13F). One of the planes defined from strain analysis of the striae in the clay gouge from the Loreto fault strikes 280° and dips 53°N. This direction, and the average trend of the rake on the striae in the clay gouge (94°), are essentially parallel to the direction of extension documented from the southeast basin fault array (Fig. 13E). There are no kinematic data from the northern Loreto fault, but its northerly strike suggests that it is a nearly pure dip-slip normal fault.

INTERPRETATION AND DISCUSSION

Structural Style of Loreto Basin

The Loreto basin is a transtensional basin that formed within a broad releasing bend of the normal and oblique-slip Loreto fault (Figs. 1, 2, and 6). Fault-kinematic data indicate that deformation and basin formation occurred by approximately east-west extension at the western margin of the Gulf of California transform-rift system (Fig. 13; Umhoefer and Stone, 1996). This is consistent with modeling studies that predict a similar orientation of extensional strain along an obliquely rifted, transtensional continental margin where the angle between the rift trend and direction of relative plate motion is about 20° (Withjack and Jamison, 1986; Fossen and Tikoff, 1993; Umhoefer and Dorsey, 1997). In this context, the strongly asymmetric geometry of the central subbasin is interpreted to record westward tilting in the hanging wall of the oblique-slip, dextral-normal Loreto fault. The deepest part of the basin is located close to the southern Loreto fault and indicates a large component of synbasinal dip-slip displacement (>1500 m; Fig. 6). Westward tilting probably resulted from extensional collapse of the hanging wall above a listric geometry in the Loreto fault (Fig. 14). We therefore consider the Loreto basin to be an oblique, transtensional half-graben basin that subsided rapidly in response to the dip-slip component of dextral-normal slip on the Loreto fault. Although many features of the Loreto basin appear similar to those of orthogonal rift basins, the very short and extremely rapid history of basin subsidence is characteristic of basin development in an overall strike-slip setting (Christie-Blick and Biddle, 1985).

The Loreto basin cannot be represented as a simple pull-apart basin because the Loreto fault terminates west of the northernmost Pliocene deposits, at a point located approximately west-southwest of the center of the Mencenares volcanic center (Fig. 1). We have considered the possibility that slip on the Loreto fault may step over to the east, and that the Pliocene Mencenares volcanic center formed along a leaky transfer fault that connects the Loreto fault to a large fault farther north and east, but this hypothesis is not supported by available data. There is no large fault north of the Mencenares complex, and no indication that fault slip is transferred through or across the volcano. This latter interpretation would require that slip on the Loreto fault steps eastward to an unknown location offshore, but there is no evidence to support this interpretation. Instead, we interpret that a large strain gradient exists on the northern part of the Loreto fault where the total slip decreases to nearly zero over a horizontal distance of ~10–15 km. The gradient of northward strain decrease is difficult to estimate because the thickness of Pliocene deposits (and thus the total amount of slip on the fault) is not known in the northern part of the basin.

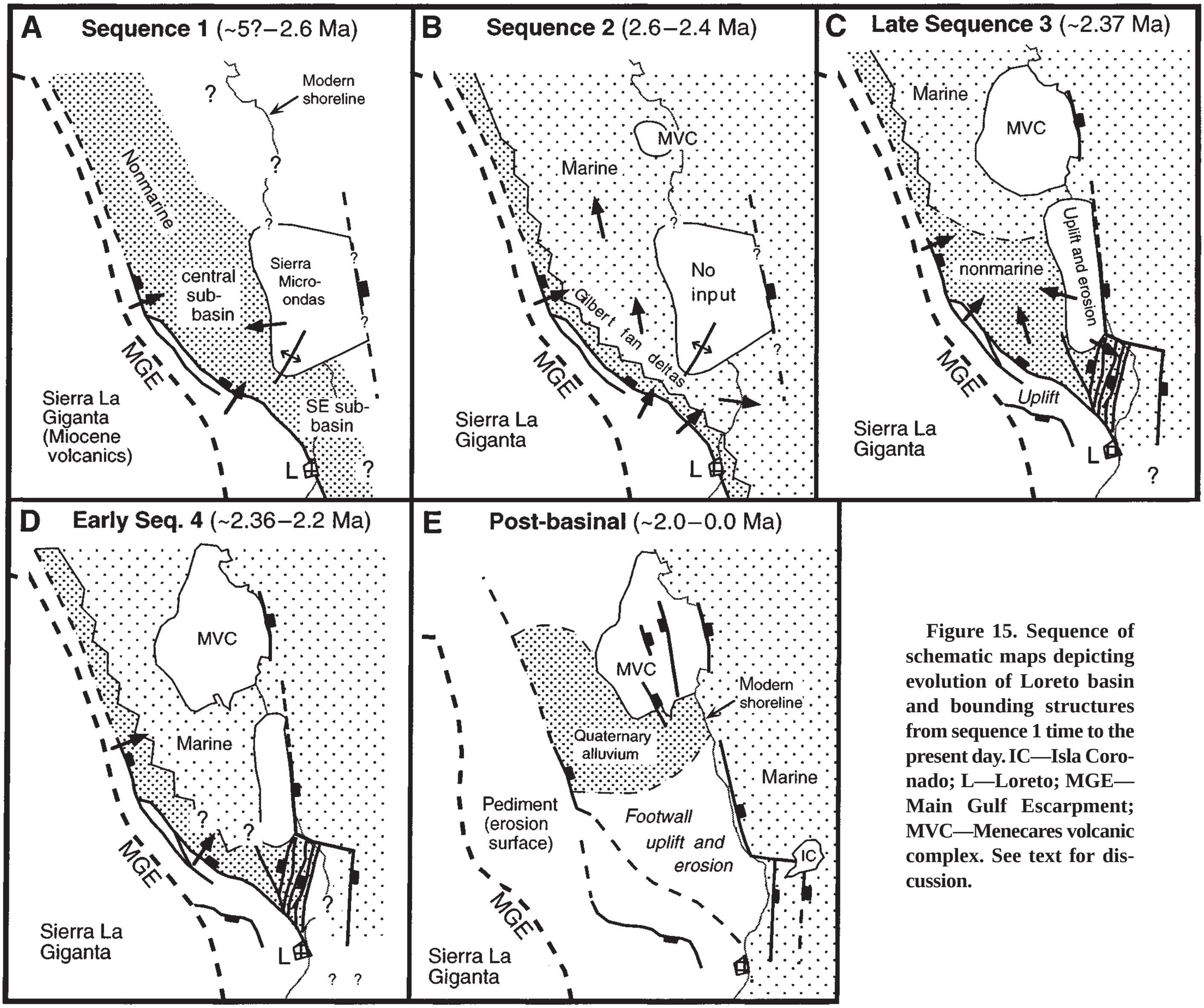

Figure 15. Sequence of schematic maps depicting evolution of Loreto basin and bounding structures from sequence 1 time to the present day. IC—Isla Coronado; L—Loreto; MGE—Main Gulf Escarpment; MVC—Menecares volcanic complex. See text for discussion.

Sequence-Stratigraphic Record of Basin Evolution

Sequence 1 records deposition in nonmarine alluvial fans during an initial, relatively slow stage of subsidence on the Loreto fault (Figs. 14A and 15A). Paleocurrent data record input from the Sierra Microondas in the east (Fig. 11), and we infer that sediment also was being shed into the basin from the footwall of the Loreto fault in the west. Although age data are not available for sequence 1 deposits, we infer that subsidence during deposition of sequence 1 probably was slower than early in sequence 2 time. The lower part of sequence 1 may be as old as 5 or 6 Ma. It therefore is possible that the early phase of deposition was initiated in latest Miocene or earliest Pliocene time when the Gulf of California first underwent significant strike-slip faulting (Lonsdale, 1989).

The abrupt marine flooding surface at the base of sequence 2 marks a major reorganization of depositional systems, sediment-dispersal paths, and basin-bounding structures (particularly the Loreto fault) that controlled patterns of subsidence and sediment input. Initial marine incursion probably resulted from an increase in the rate of fault-controlled subsidence at this time, and may have also been amplified by a rise in eustatic sea level ca. 2.62 Ma (Fig. 16). In the central subbasin, a second increase in subsidence rate occurred soon after deposition of tuff 2, the subsidence rate increasing to ~8 mm/yr (Fig. 12). As a result of this increase, 14 Gilbert delta parasequences occupying ~650 m of section in sequence 2 accumulated during a short time interval (<100 k.y.). Input from the Sierra Microondas, which represents the uplifted portion of the hanging-wall tilt block, ceased at this time and did not resume until the beginning of sequence 3 time (Figs. 14B and 15B). Footwall-derived sediment was funneled northward along the axis of the central subbasin. In the southeast subbasin, sediment was shed northward from the footwall of the Loreto fault and redirected eastward through the southeast subbasin (Figs. 11 and 15).

During deposition of sequence 2, the central subbasin underwent rapid westward tilting that produced a pronounced westward thickening and

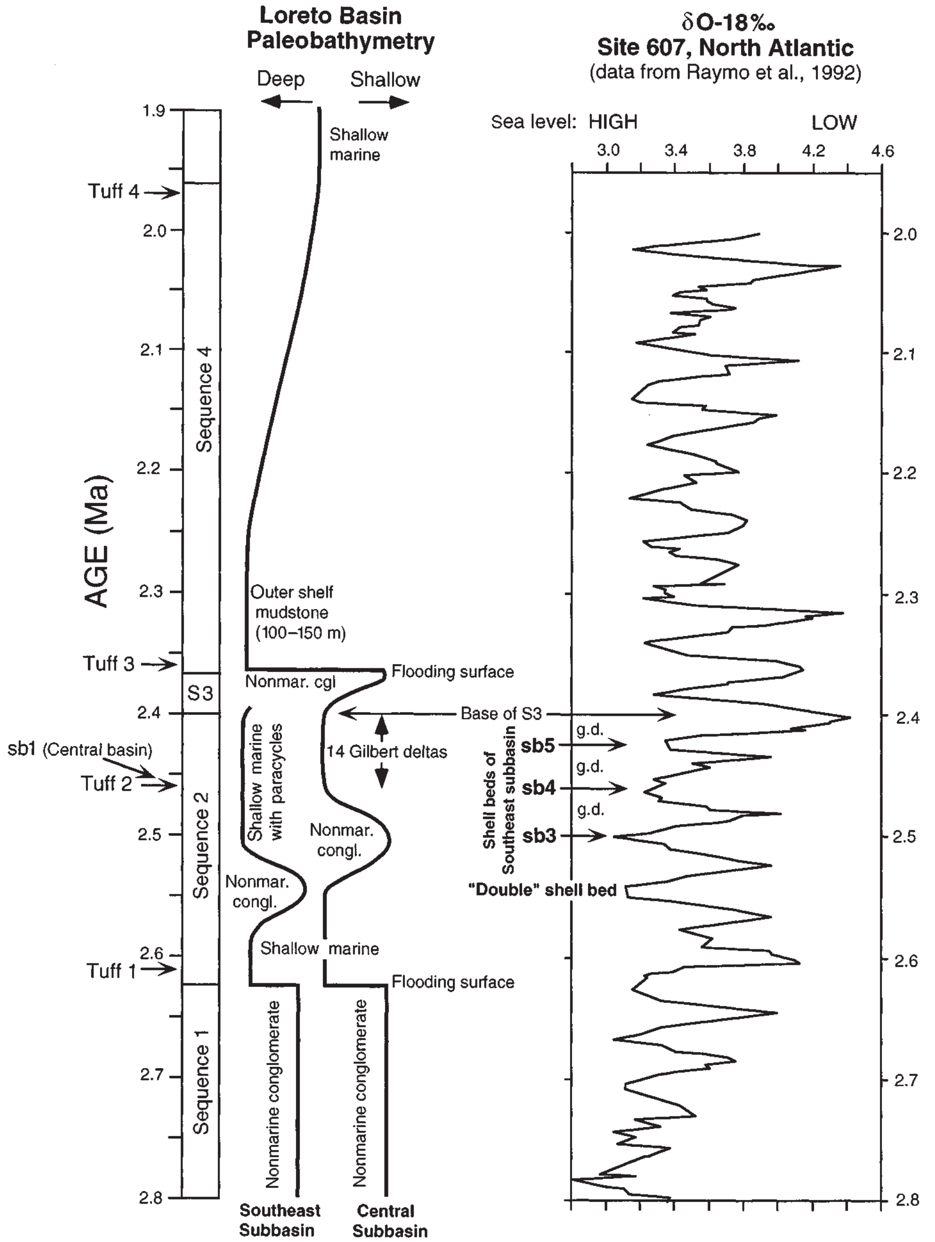

Figure 16. Comparison of Loreto basin paleobathymetry (this study) with eustatic sea-level fluctuations determined from oxygen isotopes in the North Atlantic (Raymo et al., 1992). High-frequency paracycles in the central subbasin do not match the eustatic curve, indicating tectonic control on stratigraphic evolution due to very rapid, episodic subsidence. In the southeast subbasin we observe a close correlation between number of laterally extensive shell beds and sea-level highstands, indicating a eustatic control on formation of parasequences.

coarsening of stratigraphy toward the Loreto fault. The footwall of the Loreto fault produced a correspondingly rapid influx of coarse detritus to the basin, which enabled it to stay nearly filled in spite of very rapid subsidence. In order to reconcile pronounced westward tilting with lack of sediment input from the hanging-wall dip slope, we infer that the sequence 2 stage of subsidence in the central subbasin was produced by growth of a basin-scale active syncline that formed by extensional collapse of the hanging wall above a listric normal fault (Fig. 14B; e.g., Groshong, 1989; Xiao and Suppe, 1992). This growth syncline was bounded on the east and southeast by an anticline that, due to its oblique orientation in map view, also made up the northern or northwestern margin of the southeast subbasin (Figs. 2, 14B, and 15B). Onlapping of ~600–700 m of stratigraphy onto the northern margin of the southeast subbasin (Fig. 7) indicates that this was a major structure that separated the two subbasins during most of Loreto basin evolution. On the basis of the overwhelming dominance of extensional normal faults and extensional kinematics in the area, we infer that the growth anticline formed as an extensional rollover structure, and that southeastward tilting on the southeast limb may have been controlled by a bend or step in the Loreto fault at depth. Some aspects of this interpretation remain difficult, however, because stratigraphy in the southeast subbasin reveals no evidence of synbasinal tilting within the units where we have done detailed mapping (sequence 2). This could be explained if the north-south panel for the southeast subbasin (Fig. 7) is oriented close to the strike of the growth anticline (north-northeast), in which case it would not be likely to reveal fanning dips produced by syndepositional tilting.

The transition to sequence 3 records another major change in fault-controlled subsidence and sediment-dispersal patterns. Renewed uplift of the Sierra Microondas initiated rapid influx of bioclastic carbonate material that was shed southward into the southeast subbasin and west and northwestward into the central subbasin (Figs. 11 and 15C). In the southeast subbasin, intrabasinal tilting and erosion produced a low-angle unconformity at the base of sequence 3 (Fig. 9). In the central subbasin, where subsidence was extremely rapid, the transition to sequence 3 occurred by progradation of bioclastic Gilbert-type fan deltas to produce a strong downlapping geometry with no unconformity (Fig. 6). Initiation of sequence 3 records several major changes in structural style: (1) initiation of the normal fault on the east side of the Sierra Microondas; (2) progradation of carbonates eroded from this uplifted area into the flanking subbasins; (3) slowing of slip on the Loreto fault and initiation of the southeast fault array; and (4) change in subsidence geometry in the central subbasin from markedly asymmetric to nearly symmetrical (Fig. 14C). The latter change in subsidence geometry may have resulted from continued growth of the basin-scale growth syncline coincident with substantially slowed slip rate on the Loreto fault, resulting in uniform rates of subsidence (and uniform cross-basin thickness of sequence 3) across the central subbasin (Fig. 6). We infer that subsidence rate in the central subbasin slowed by the end of sequence 3 time, resulting in progradation of nonmarine alluvial fans over marine deposits (Figs. 12B and 15C).

Progradation of nonmarine gravel in the upper part of sequence 3 and the subsequent abrupt onset of distal marine conditions (base of sequence 4) are interpreted to be the result of changes in subsidence rate (Fig. 12B). Although gravel progradation could be explained by either slowing of accommodation production or an increase in the rate of sediment input, the sudden foundering of fluvial environments to >100 m water depth can only be explained by an abrupt subsidence event. This cannot be solely the product of eustatic sea-level rise because the section does not record a return to shallow-marine or fluvial conditions within the appropriate time frame (Fig. 16). Subsidence therefore must have been unsteady during the time interval between tuffs 2 and 3. We infer that the stratigraphic architecture bracketed between tuffs 2 and 3 in the central subbasin was produced primarily by variations in the rate of subsidence on the Loreto fault, and the rapid shift of fault slip to the Sierra Microondas fault and southeast fault array (Figs. 6, 8, and 12B). Gilbert-delta deposition was initiated by a sharp increase in subsidence rate that coincided with deposition of tuff 2 (see also Dorsey et al., 1995). Near the end of sequence 3 time, slowing of subsidence caused progradation of nonmarine conglomerate along the basin axis.

The transition to sequence 4 was markedly different in the central and southeast subbasins (Fig. 15D). In the central subbasin, the basin floor foundered and subsided quickly to water depths of 100–150 m. This probably resulted from a final pulse of very rapid slip on the Loreto fault. In the southeast subbasin, faulting, uplift, and erosion took place during foundering of the central subbasin, as recorded in the southeast fault array, angular unconformity, and fanning-dip section in the southeast subbasin. Some time later, sedimentation resumed in the southeast subbasin in the form of in situ shallow-marine carbonate deposition adjacent to highlands in the Sierra Microondas and newly emerged portions of the previously marine southeast subbasin. Finally, the Loreto basin has been progressively uplifted and eroded since ca. 2 Ma, in the footwalls of modern, active coastal and nearshore faults (Fig. 15E).

Tectonic vs. Eustatic Controls on Parasequence Cyclicity

The evolution of the central subbasin differed markedly from that of the southeast subbasin. In sequences 2, 3, and 4, we document notable contrasts in thickness, sedimentology, type of sequence boundaries, rate of sediment accumulation, and number and stacking pattern of parasequences, all of which were controlled by contrasting structural behavior of the two areas. The central subbasin formed in a deep, rapidly subsiding growth syncline that formed in the hanging-wall tilt block close to the Loreto fault, while the southeast subbasin formed in a structurally shallower position on the southeast side of an active anticline that separated the two subbasins (Figs. 14B and 15B). Due to the structurally perched position of the southeast subbasin, it underwent faulting, uplift, and erosion during a time (early sequence 4) when the central subbasin foundered abruptly to deep water depths and then slowly filled with marine mudstone.

The contrasting structural behavior of the two subbasins produced significantly different subsidence rates during sequence 2 time: ~8 mm/yr in the central subbasin and ~1.5 mm/yr in the southeast subbasin. The two subbasins also contain, within sequence 2, a significantly different number of progradational parasequences capped by hiatal transgressive shell beds: 14 in the central subbasin compared to 4 in the southeast subbasin (Fig. 8). Figure 16 shows paleobathymetry for the two Loreto subbasins compared to temporal variations in oxygen isotopes from the North Atlantic Ocean (data from Raymo et al., 1992), which are used here as a proxy for eustatic sea level. Although it is easy to reconstruct changes in paleoenvironments and paleobathymetry through time, it is difficult to determine whether those changes were controlled by variations in eustatic sea level, rate of basin subsidence, or sediment supply. This problem is analyzed in the following.

Sequence 2 in the central subbasin contains 14 Gilbert deltas (paracycles), bracketed between tuff 2 and the base of sequence 3, which record 14 episodes of deltaic progradation and marine flooding (Fig. 16). These paracycles accumulated during ~1.5 cycles of eustatic sea-level change as interpreted from the isotope excursions (41 k.y. per cycle). This obvious mismatch indicates that global eustatic fluctuations did not exert the main control on Gilbert delta cyclicity in the central subbasin. On the basis of this and other considerations, we infer that high-frequency stratigraphic cycles in the central subbasin were produced by episodic fault-controlled subsidence possibly related to temporal clustering of earthquakes (Dorsey et al., 1997b). In this model, rapid progradation of gravelly Gilbert deltas occurred during periods of slow or negligible slip and slow subsidence on the Loreto fault. We infer that rapid marine transgression and deposition of capping shell beds directly on delta-plain deposits (topsets) occurred during short bursts of extremely rapid tectonic subsidence on the Loreto fault, which produced back tilting of alluvial fans, decrease of channel gradients, and temporary sediment starvation in the nearshore marine realm. A summary of competing hypotheses and reasons for favoring this model was presented in Dorsey et al. (1997b). From this we conclude that parasequences in the central subbasin were produced by very rapid, episodic tectonic subsidence that effectively overwhelmed the influence of eustatic sea-level changes.

A strikingly different pattern is seen in the southeast subbasin, where we observe four laterally continuous shell beds in sequence 2 (Figs. 7 and 8) that appear to match four highstands of eustatic sea level between tuff 1 and the base of sequence 3 (Fig. 16). We favor a correlation of these shell beds to the marine isotope curve in part because it is unlikely that the relatively slow subsidence rate of ~1.5 mm/yr would be fast enough to swamp out the eustatic signal in a marine setting. Variations in sediment supply cannot be ruled out, but the close match with the marine isotope record supports the interpretation that stratigraphic cyclicity of shell beds in the southeast subbasin was controlled by eustasy. The lowest of these is the double shell bed (dsb), a hiatal shell concentration that lies stratigraphically between two units of nonmarine conglomerate in the lower part of sequence 2 (Figs. 7, 8, and 16). We propose that the double shell bed accumulated during a eustatic sea-level rise that briefly overwhelmed gravel progradation and produced a short interval of marine flooding. We further suggest that shell bed 1 in the central subbasin correlates with shell bed 4 in the southeast subbasin. This correlation is supported by the anomalously wide lateral extent of shell bed 1 in the central subbasin compared to other delta-capping shell beds in that area, and implies that it is in part a product of eustatic sea-level rise.

The preceding summary helps to highlight important contrasts in the behavior of the two subbasins during deposition of sequence 2. In the central subbasin, extremely rapid subsidence (~8 mm/yr), combined with strong episodic variations in subsidence rate, overwhelmed rates of eustatic sea-level change and exerted the dominant control on internal stratigraphic cyclicity. In the southeast subbasin, subsidence was slower (~1.5 mm/yr), and eustatic sea-level change exerted the dominant control on progradation and retrogradation of parasequences. It is interesting to note that our model for the southeast subbasin resembles the behavior represented in recently published models for half-graben depocenters located close to bounding normal faults, in which high-frequency sea-level change is superimposed on background basin subsidence, and eustasy exerts the main control on internal stratigraphic cyclicity (e.g., Gawthorpe et al., 1994; Hardy and Gawthorpe, 1998). In our model for the central subbasin, by contrast, internal stratigraphic variations are driven by very high frequency episodic subsidence and there is virtually no expression of eustatic sea-level change. This appears to represent an end member in the possible range of interactions between basin subsidence and eustasy in tectonically active basins. Based on subsidence rates in the two subbasins, we estimate that maximum rates of eustatic sea-level change may have been between ~2 and 8 mm/yr. Hypothetically, a sea-level rise of 100 m occurring in 20 k.y. (~one-half of the 41 k.y. cyclicity recorded in Fig. 16) represents a rate of rise of 5 mm/yr. Although the magnitudes of sea-level change during Pliocene time are not well known, changes on the order of 80–100 m are considered reasonable (Raymo et al., 1989, 1992; Blanchon and Shaw, 1995), and thus rates of change of ~4–5 mm/yr seem reasonable.

Sequence Stratigraphy in Tectonically Active Basins

In traditional models of sequence stratigraphy, a sequence is defined as "a relatively conformable succession of genetically related strata bounded by unconformities and their correlative conformities" (Van Wagoner et al., 1988, p. 39). Type 1 sequence boundaries are erosional unconformities produced by a fall in relative sea level, stream incision, and a basinward shift in facies. Type 2 sequence boundaries also are erosional unconformities, but they lack evidence for subaerial erosion, stream rejuvenation, and basinward shift in facies in the marine realm. Highstands, lowstands, and lateral shifting of the shoreline result from the interplay between rate of production or loss of accommodation space (traditionally attributed to rate of eustatic sea-level rise or fall) and rate of sediment input. These and related concepts were developed and refined for passive continental margins where rates of subsidence and sediment input may be several orders of magnitude slower that those of tectonically active basins (e.g., Vail et al., 1977; Van Wagoner et al., 1988; Posamentier et al., 1988). This contrast is especially acute for strike-slip related basins, which commonly experience subsidence rates ≥1 mm/yr (1 m/1 k.y.) (Johnson et al., 1983; Christie-Blick and Biddle, 1985; Pitman and Andrews, 1985).

Early concepts of sequence stratigraphy were later refined by emphasizing the concept that regional basin subsidence can and often does dominate the production of accommodation space, and in concert with variations in sediment supply, may exert the main control on development of stratigraphic sequences and their boundaries (Galloway, 1989; Embry, 1989; Jordan and Flemings, 1991; Coakley and Watts, 1991; Sinclair et al., 1991; Posamentier and Allen, 1993). More recently it has been recognized that in tectonically active settings dominated by rapid local subsidence, basins may undergo a continual rise in relative sea level through time, and stratigraphic sequences may be bounded by nonerosive, composite surfaces of marine flooding, maximum transgression and downlap (Gawthorpe et al., 1994, 1997; Dart et al., 1994; Burns et al., 1997; Hardy and Gawthorpe, 1998). In these cases, the dominant architectural features of the stratigraphy may reflect major subsidence or basin-foundering events in the basin. Similarly, we have found it both necessary and useful to define sequences in the Loreto basin using refined criteria that depart somewhat from those of the traditional sequence-stratigraphic paradigm.

The sequence 1–2 boundary and the 3–4 boundary in the central subbasin are abrupt surfaces of marine flooding that mark major changes in relative sea level, stratigraphic architecture, and parasequence stacking patterns. There is no evidence for subaerial erosion or lowering of relative sea level at these contacts; instead they record pronounced and sudden relative sea-level rise. Our work shows that these boundaries are the most internally consistent and useful surfaces for mapping and defining sequences in the Loreto basin, consistent with the concept of genetic stratigraphic sequences of Galloway (1989). The lack of erosional unconformities at these boundaries reflects the very rapid subsidence history of the Loreto basin. In the central subbasin, where sequence boundaries are not unconformities, subsidence rates outpaced eustatic sea-level fluctuations and the basin underwent a continual rise in relative sea level. The evolution of the central subbasin therefore is recognized as being punctuated by major basin-foundering events that produced distinctive sequence-bounding marine flooding surfaces.

The sequence 2–3 boundary is an unconformity in some locations, a conformable transition in others, and in the western half of the central subbasin it is a parasequence boundary similar to others preserved in the thick western part of the basin (Fig. 6). In the western part of the central subbasin the parasequence stacking pattern does not require a sequence boundary, and in that area by that definition we would not subdivide sequences 2 and 3. However, several other observations bear on this question. First, the base of sequence 3 becomes a surface of substantial stratigraphic omission on the eastern margin of the central subbasin, where carbonates directly overlie Miocene volcanic basement rocks of the Sierra Microondas (Fig. 6). In this case the sequence boundary is best displayed around the extreme margins of the basin, but within most parts of the central subbasin this transition would not be picked as a sequence boundary. We therefore emphasize the concept of the sequence-bounding unconformity and its correlative conformity, which is appropriate due to the subsidence-dominated behavior of the central subbasin during deposition of sequences 2 and 3. Second, the change from sequence 2 to sequence 3 records profound changes in provenance, sediment dispersal, and uplift and erosion of the eastern source area, all of which resulted from reorganization of basin-margin faults and large-scale patterns of tilting and erosion. Finally, this boundary in the central subbasin is correlable with a low-angle erosional unconformity in the southeast subbasin. Thus, the sequence 2–3 boundary records one of the most important tectonic events in the Loreto basin, and the influence of this change is well displayed in the stratigraphic record wherever hanging-wall–derived sediments are preserved.

CONCLUSIONS

The Pliocene Loreto basin is an oblique, transtensional half-graben basin that formed in a zone of transtensional deformation along the active transform-rift plate boundary in the Gulf of California. The basin probably was initiated in early Pliocene time and underwent a rapid phase of subsidence and filling between ca. 2.6 and 2.0 Ma. Basin formation and westward tilting occurred in response to east-west extension and the dip-slip component of oblique slip on the dextral-normal southern Loreto fault. The central subbasin is located close to the Loreto fault and underwent a very short lived pulse of extremely rapid subsidence (~8 mm/yr) between ca. 2.46 and 2.36 Ma during deposition of sequences 2 and 3. The southeast subbasin subsided more slowly (~1–2 mm/yr) in a structural accommodation zone, and was strongly deformed by closely spaced west-dipping normal faults in the southeast fault array.

Sedimentary deposits of the Loreto basin comprise a diverse assemblage of nonmarine to marine, coarse- to fine-grained siliciclastic and carbonate deposits. The stratigraphy is divided into four sequences that record four distinct phases of fault-controlled basin evolution. The sequence 1–2 boundary is a marine flooding surface that formed by marine incursion of a previously nonmarine basin in response to increased subsidence rate and reorganization of basin-bounding faults. Sequence 2 is characterized by siliciclastic, marginal marine Gilbert-type fan deltas that were fed by steep, footwall-sourced alluvial fans. The sequence 2–3 and 3–4 boundaries vary substantially between the central and southeast subbasins. In the southeast subbasin, these boundaries are slightly to strongly erosional unconformities, but in the central subbasin they are conformable surfaces of stratigraphic downlap (2–3) and pronounced marine flooding (3–4). The marked difference in sequence boundaries is a direct result of contrasting accommodation space: the southeast subbasin underwent subtle to strong uplift and erosion during episodes of structural transition, whereas the central subbasin underwent continued subsidence or basin foundering.

We are able to distinguish between tectonic and eustatic controls on stratigraphic signatures for sequence 2 in the two subbasins, by comparing the well-constrained chronology of paracycles and shell beds with oxygen-isotope records from North Atlantic Ocean Drilling Program cores. In the central subbasin, very rapid subsidence (~8 mm/yr) outpaced the rate of sea-level fluctuations, and the 14 paracycles of sequence 2 provide a record of episodic tectonic subsidence with virtually no eustatic signal. In the southeast subbasin, however, net subsidence rate was sufficiently slower (1–2 mm/yr) that sea-level fluctuations exerted the main control on parasequence evolution.

Deformation within the basin first occurred ca. 2.4 Ma near the sequence 2–3 transition, as recorded in a low-angle unconformity in the southeast subbasin and a growth syncline in the lower part of sequence 3 in the central subbasin. This localized deformation was produced by initiation of the southeast Loreto fault array and the beginning of a shift of faulting from the Loreto fault to a coastal fault system. The southeast fault array became more active immediately after sequence 3 time, producing an angular unconformity and fanning dips at the base of sequence 4 in the southeast subbasin. Initiation of the southeast fault array was accompanied by a decrease in slip rate on the southern Loreto fault and related progradation of the shoreline to the north and east. During latest Pliocene to Quaternary time, faulting has taken place along the northern Loreto fault, the Sierra Microondas fault, and a linked east-west fault that apparently projects offshore to Coronado Island.

ACKNOWLEDGMENTS

Financial support of this study was provided by the National Science Foundation grants EAR-9117269 and EAR-956506 and the Petroleum Research Fund of the American Chemical Society. We gratefully acknowledge many productive and insightful conversations with Susan Kidwell, Larry Mayer, Jim Ingle, Bob Douglas, Jorge Ledesma, Enrique Nava, Peter Falk, and Andy Stone. Bob Douglas kindly provided analyses and interpretations of benthic fauna for depth determination of the El Troquero Formation. We thank Peter Falk for contributing paleocurrent data from the central subbasin. We express our gratitude to Miguel Valdes and the people of Loreto for years of support and friendship during this study.

REFERENCES CITED

Anderson, C. A., 1950, Geology of islands and neighboring land areas: Part I of the 1940 E. W. Scripps Cruise to the Gulf of California: Geological Society of America Memoir 43, part 1, p. 1–53.

Angelier, J., Colletta, B., Chorowicz, J., Ortlieb, L., and Rangin, C., 1981, Fault tectonics of the Baja California Peninsula and the opening of the Sea of Cortez, Mexico: Journal of Structural Geology, v. 3, p. 347–357.

Angevine, C. L., Heller, P. L., and Paola, C., 1990, Quantitative sedimentary basin modelling: American Association of Petroleum Geologists Continuing Education Course Note Series no. 32, 133 p.

Axen, G., 1995, Extensional segmentation of the Main Gulf Escarpment, Mexico and United States: Geology, v. 23, p. 515–518.

Bigioggero, B., Chiesa, S., Zanchi, A., Montrasio, A., and Vezzoli, L., 1995, The Cerro Mencenares volcanic center, Baja California Sur; source and tectonic control on post-subduction magmatism within the Gulf Rift: Geological Society of America Bulletin, v. 107, p. 1108–1122.

Blanchon, P., and Shaw, J., 1995, Reef drowning during the last deglaciation: Evidence for catastrophic sea-level rise and ice-sheet collapse: Geology, v. 23, p. 4–8.

Bosworth, W., 1985, Geometry of propagating continental rifts: Nature, v. 316, p. 625–627.

Burns, B. A., Heller, P. L., Marzo, M., and Paola, C., 1997, Fluvial response in a sequence stratigraphic framework: Example from the Montserrat fan delta, Spain: Journal of Sedimentary Research, v. 67, p. 311–321.

Christie-Blick, N., and Biddle, K. T., 1985, Deformation and basin formation along strike slip faults, *in* Biddle, K. T., and Christie-Blick, N., eds., Strike-slip deformation, basin formation, and sedimentation: Society of Economic Paleontologists and Mineralogists Special Publication 37, p. 1–34.

Coakley, B. J., and Watts, A. B., 1991, Tectonic controls on the development of unconformities; the North Slope, Alaska: Tectonics, v. 10, p. 101–130.

Curray, J. R., and Moore, D. G., 1984, Geologic history of the Gulf of California, *in* Frizzell, V. A., ed., Geology of the Baja California Peninsula: Bakersfield, California, Pacific Section, Society of Economic Paleontologists and Mineralogists, p. 17–36.

Dart, C. J., Collier, R. E. L., Gawthorpe, R. L., Keller, J. V. A., and Nichols, G., 1994, Sequence stratigraphy of (?) Pliocene-Quaternary synrift, Gilbert-type fan deltas, northern Peloponnesos, Greece: Marine and Petroleum Geology, v. 11, p. 545–560.

Dorsey, R. J., 1997, Origin and significance of rhodolith-rich strata in the Punta el Bajo section, southeastern Pliocene Loreto basin, *in* Johnson, M. E., and Ledesma-Vasquez, J., eds., Pliocene carbonates and related facies flanking the Gulf of California, Baja California Sur, Mexico: Geological Society of America Special Paper 318, p. 119–126.

Dorsey, R. J., and Burns, B. A., 1994, Regional stratigraphy, sedimentology and tectonic significance of Oligocene-Miocene sedimentary and volcanic rocks, northern Baja California, Mexico: Sedimentary Geology, v. 88, p. 231–251.

Dorsey, R. J., and Kidwell, S. M., 1999, Mixed carbonate-siliciclastic sedimentation on a tectonically active margin: Example from the Pliocene of Baja California Sur, Mexico: Geology, v. 27, p. 935–938.

Dorsey, R. J., Umhoefer, P. J., and Renne, P. R., 1995, Rapid subsidence and stacked Gilbert-type fan deltas, Pliocene Loreto Basin, Baja California Sur, Mexico: Sedimentary Geology, v. 98, p. 181–204.

Dorsey, R. J., Stone, K. A., and Umhoefer, P. J., 1997a, Stratigraphy, sedimentology, and tectonic development of the southeastern Loreto basin, Baja California Sur, Mexico, *in* Johnson, M. E., and Ledesma-Vasquez, J., eds., Pliocene carbonates and related facies flanking the Gulf of California, Baja California Sur, Mexico: Geological Society of America Special Paper 318, p. 83–109.

Dorsey, R. J., Umhoefer, P. J., and Falk, P., 1997b, Earthquake clustering and stacked Gilbert-type fan deltas in the Pliocene Loreto Basin, Baja California Sur, Mexico: Geology, v. 25, p. 679–682.

Durham, J. W., 1950, Megascopic paleontology and marine stratigraphy: Part 2 of the 1940 E. W. Scripps cruise to the Gulf of California: Geological Society of America Memoir 43, 216 p.

Embry, A. F., 1989, A tectonic origin for third-order depositional sequences in extensional basins: Implications for basin modeling, *in* Cross, T. A., ed., Quantitative dynamic stratigraphy: Englewood Cliffs, New Jersey, Prentice-Hall, p. 491–501.

Falk, P. D., 1996, Stratigraphy and sedimentology of Pliocene fan-delta deposits, Loreto basin, Baja California Sur, Mexico [M.S. thesis]: Flagstaff, Northern Arizona University, 173 p.

Falk, P., and Dorsey, R. J., 1998, Rapid development of gravelly high-density turbidity currents in marine Gilbert-type fan deltas, Loreto basin, Baja California Sur, Mexico: Sedimentology, v. 45, p. 331–349.

Fossen, H., and Tikoff, B., 1993, The deformation matrix for simultaneous simple shearing, pure shearing, and volume change, and its application to transpression/transtension tectonics: Journal of Structural Geology, v. 15, p. 413–422.

Galloway, W. E., 1989, Genetic stratigraphic sequences in basin analysis 1: Architecture and genesis of flooding-surface bounded depositional units: American Association of Petroleum Geologists Bulletin, v. 73, p. 125–142.

Gastil, R. G., Phillips, R. P., and Allison, E. C., 1975, Reconnaissance geology of the state of Baja California: Geological Society of America Memoir 140, 170 p.

Gawthorpe, R. L., and Colella, A., 1990, Tectonic controls on coarse-grained delta depositional systems in rift basins, *in* Colella, A., and Prior, D. B. eds., Coarse-grained deltas: International Association of Sedimentologists Special Publication 10, p. 113–127.

Gawthorpe, R. L., Fraser, A. J., and Collier, R. E., 1994, Sequence stratigraphy in active extensional basins: Implications for the interpretation of ancient basin-fills: Marine and Petroleum Geology, v. 11, p. 642–658.

Gawthorpe, R. L., Sharp, I., Underhill, J. R., and Gupta, S., 1997, Linked sequence stratigraphic and structural evolution of propagating normal faults: Geology, v. 25, p. 795–798.

Groshong, R. H., 1989, Half-graben structures; balanced models of extensional fault-bend folds: Geological Society of America Bulletin, v. 101, p. 96–105.

Hardy, S., and Gawthorpe, R. L., 1998, Effects of variations in fault slip rate on sequence stratigraphy in fan deltas: Insights from numerical modeling: Geology, v. 26, p. 911–914.

Hausback, B. P., 1984, Cenozoic volcanic and tectonic evolution of Baja California, Mexico, *in* Frizzell, V. A., ed., Geology of the Baja California Peninsula: Bakersfield, California, Pacific Section, Society of Economic Paleontologists and Mineralogists, p. 219–236.

Heller, P. L., and Paola, C., 1992, The large-scale dynamics of grain-size variation in alluvial basins, 2: Application to syntectonic conglomerate. Basin Research, v. 4, p. 91–102.

Jervey, M. T., 1988, Quantitative geological modeling of siliciclastic rock sequences and their seismic expression, *in* Wilgus, C. K., Hastings, B. S., Kendall, C. G. S. C., Posamentier, H. W., Ross, C. A., and Van Wagoner, J. C., eds., Sea-level changes: An integrated approach: Society of Economic Paleontologists and Mineralogists Special Publication 42, p. 47–69.

Johnson, N. M., Officer, C. B., Opdyke, N. D., Woodard, G. D., Zeitler, P. K., and Lindsay, E. H., 1983, Rates of late Cenozoic tectonism in the Vallecito–Fish Creek basin, western Imperial Valley, California: Geology, v. 11, p. 664–667.

Jordan, T. E., and Flemings, P. B., 1991, Large-scale stratigraphic architecture, eustatic variation, and unsteady tectonism: A theoretical evaluation: Journal of Geophysical Research, v. 96, p. 6681–6699.

Koltermann, C. E., and Gorelick, S. M., 1992, Paleoclimate signature in terrestrial flood deposits: Science, v. 256, p. 1775–1782.

Larson, R. L., 1972, Bathymetry, magnetic anomalies, and plate tectonic history of the mouth of the Gulf of California: Geological Society of America Bulletin, v. 83, p. 3345–3359.

Leeder, M. R., and Gawthorpe, R. L., 1987, Sedimentary models for extensional tilt-block/half-graben basins, *in* Coward, M. P., Dewey, J. F., and Hancock, P. L., eds., Continental extensional tectonics: Geological Society of America Special Publication 28, p. 139–152.

Lonsdale, P., 1989, Geology and tectonic history of the Gulf of California, *in* Winterer, E. L., Hussong, D. M., and Decker, R. W., eds., The eastern Pacific Ocean and Hawaii: Boulder, Colorado, Geological Society of America, Geology of North America, v. N, p. 499–521.

Marrett, R., and Allmendinger, R. W., 1990, Kinematic analysis of fault-slip data: Journal of Structural Geology, v. 12, p. 973–986.

Mayer, L., and Vincent, K., 1999, Active tectonics of the Loreto area, Baja California Sur, Mexico: Geomorphology, v. 27, p. 243–255.

McLean, H., 1988, Reconnaissance geologic map of the Loreto and part of the San Javier quadrangles, Baja California Sur, Mexico: U.S. Geological Survey Map MF-2000, scale 1:50 000

McLean, H., 1989, Reconnaissance geology of a Pliocene marine embayment near Loreto, Baja California Sur, Mexico, *in* Abbot, P. L., ed., Geologic Studies in Baja California, Field Trip Guidebook: Pacific Section, Society of Economic Paleontologists and Mineralogists, v. 63, p. 17–25.

Nava-Sanchez, E. H., 1997, Modern fan deltas of the west coast of the Gulf of California, Mexico [Ph.D. dissertation]: Los Angeles, University of Southern California, 229 p.

Nemec, W., 1990, Aspects of sediment movement on steep delta slopes, *in* Colella, A., and Prior, D. B., eds., Coarse-grained deltas: International Association of Sedimentologists Special Publication 10, p. 29–73.

Piazza, M., and Robba, E, 1994, Pectinids and oysters from the Pliocene Loreto basin (Baja California Sur, Mexico): Rivista Italiana Paleontografia e Stratigrafia, v. 100, p. 33–69.

Pitman, W. C., and Andrews, J. A., 1985, Subsidence and thermal history of small pull-apart basins, *in* Biddle, K. T., and Christie-Blick, N., eds., Strike-slip deformation, basin formation, and sedimentation: Society of Economic Paleontologists and Mineralogists Special Publication 37, p. 45–49.

Posamentier, H. W., and Allen, G. P., 1993, Variability of the sequence stratigraphic model: Effects of local basin factors. Sedimentary Geology, v. 86, p. 91–109.

Posamentier, H. W., Jervey, M. T., and Vail, P. R., 1988, Eustatic controls on clastic deposition 1: Conceptual framework, *in* Wilgus, C. K., Hastings, B. S., Kendall, C. G. S. C., Posamentier, H. W., Ross, C. A., and Van Wagoner, J. C., eds., Sea-level changes: An integrated approach: Society of Economic Paleontologists and Mineralogists Special Publication 42, p. 109–124.

Raymo, M. E., Ruddiman, W. F., Backman, J., Clement, B. M., and Martinson, D. G., 1989, Late Pliocene variation in Northern Hemisphere ice sheets and North Atlantic Deep Water circulation: Paleoceanography, v. 4, p. 413–446.

Raymo, M. E., Hodell, D., and Jansen, E., 1992, Response of deep ocean circulation to initiation of Northern Hemisphere glaciation (3–2 Ma): Paleoceanography, v. 7, p. 645–672.

Rosendahl, B. R., 1987, Architecture of continental rifts with special reference to East Africa: Annual Review of Earth and Planetary Sciences, v. 15, p. 445–503.

Sawlan, M. G., 1991, Magmatic evolution of the Gulf of California rift, *in* Dauphin, J. P., and Simoneit, B. R. T., eds., The Gulf and Peninsular Province of the Californias: American Association of Petroleum Geologists Memoir 47, p. 301–375.

Sinclair, H. D., Coakley, B. J., Allen, P. A., and Watts, A. B., 1991, Simulation of foreland basin stratigraphy using a diffusion model of mountain belt uplift and erosion; an example from the Central Alps, Switzerland: Tectonics, v. 10, p. 599–620.

Steckler, M. S., and Watts, A. B., 1978, Subsidence of the Atlantic-type continental margin off New York: Earth and Planetary Science Letters, v. 41, p. 1–13.

Stock, J. M., and Hodges, K. V., 1989, Pre-Pliocene extension around the Gulf of California and the transfer of Baja California to the Pacific plate: Tectonics, v. 8, p. 99–115.

Teyssier, C., Tikoff, B., and Markley, M., 1995, Oblique plate motion and continental tectonics: Geology, v. 23, p. 447–450.

Umhoefer, P. J., and Dorsey, R. J., 1997, Translation of terranes: Lessons from central Baja California, Mexico: Geology, v. 25, p. 1007–1010.

Umhoefer, P. J., and Stone, K. A., 1996, Description and kinematics of the southeast Loreto basin fault array, Baja California Sur, Mexico: A positive field test of oblique-rift models: Journal of Structural Geology, v. 18, p. 595–614.

Umhoefer, P. J., Dorsey, R. J., and Renne, P., 1994, Tectonics of the Pliocene Loreto basin, Baja California Sur, Mexico, and the evolution of the Gulf of California: Geology, v. 22, p. 649–652.

Umhoefer, P. J., Mayer, L., and Dorsey, R. J., 1997, Rift segmentation on the margin of the Gulf of California near Loreto, Baja California peninsula, Mexico: Geological Society of America Abstracts with Programs, v. 29, no. 6, p. A-481.

Vail, P. R., Mitchum, R. M., and Thompson, S., 1977, Seismic stratigraphy and global sea level, part 3: Relative changes of sea level from coastal onlap, *in* Payton, C. E., ed., Seismic stratigraphy: Applications to hydrocarbon exploration: American Association of Petroleum Geologists Memoir 26, p. 63–81.

van Andel, T. H., 1964, Recent marine sediments of the Gulf of California, *in* van Andel, T. H., and Shor, G. G., eds., Marine geology of the Gulf of California: American Association of Petroleum Geologists Memoir 3, p. 216–310.

Van Wagoner, J. C., Posamentier, H. W., Mitchum, R. M., Vail, P. R., Sarg, J. F., Loutit, T. S., and Hardenbol, J., 1988, An overview of the fundamentals of sequence stratigraphy and key definitions, *in* Wilgus, C. K., Hastings, B. S., Kendall, C. G. S. C., Posamentier, H. W., Ross, C. A., and Van Wagoner, J. C., eds., Sea-level changes: An integrated approach: Society of Economic Paleontologists and Mineralogists Special Publication 42, p. 39–45.

Withjack, M. O., and Jamison, W. R., 1986, Deformation produced by oblique rifting: Tectonophysics, v. 126, p. 99–124.

Xiao, H., and Suppe, J., 1992, Origin of rollover: American Association of Petroleum Geologists Bulletin, v. 76, p. 509–529.

Zanchi, A., 1991, Tectonic and liquefaction structures in the Loreto basin, Baja California (Mexico): Synsedimentary deformation along a fossil fault plane: Geodinamica Acta, v. 5, p. 187–202.

Zanchi, A., 1994, The opening of the Gulf of California near Loreto, Baja California, Mexico: From basin and range extension to transtentional tectonics: Journal of Structural Geology, v. 16, p. 1619–1639.

Manuscript Received by the Society June 15, 1998
Revised Manuscript Received March 30, 1999
Manuscript Accepted April 23, 1999

Printed in U.S.A.